Early View publication on www.interscience.wiley.com
(issue and page numbers not yet assigned;
citable using Digital Object Identifier – **DOI**)

phys. stat. sol. (b), 1–26 (2008) / **DOI** 10.1002/pssb.200743315

physica status solidi b
www.pss-b.com
basic solid state physics

Review Article

Fe in III–V and II–VI semiconductors

Enno Malguth[*, 1, 2], **Axel Hoffmann**[1], **and Matthew R. Phillips**[2]

[1] Institut für Festkörperphysik, Technische Universität Berlin, Hardenbergstraße 36, 10623 Berlin, Germany
[2] Microstructural Analysis Unit, University of Technology, Sydney, Broadway, NSW 2007, Australia

Received 11 July 2007, revised 7 November 2007, accepted 20 November 2007
Published online 1 February 2008

PACS 71.70.Ej, 71.70.Gm, 75.50.Pp, 76.30.Fc, 78.40.Fy

[*] Corresponding author: e-mail malguth@physik.tu-berlin.de, Phone: +49-30-31424440, Fax: +49-30-31422064

Many theoretical and experimental studies deal with the realization of room-temperature ferromagnetism in dilute magnetic semiconductors (DMS). However, a detailed quantitative understanding of the electronic properties of transition metal doped semiconductors has often been neglected. This article points out which issues concerning electronic states and charge transfers need to be considered using Fe as an example. Methods to address these issues are outlined, and a wealth of data on the electronic properties of Fe doped III–V and II–VI compound semiconductors that have been obtained over a few decades is reviewed thoroughly. The review is complemented by new results on the effective-mass-like state consisting of a hole bound to Fe^{2+} forming a shallow acceptor state.

The positions of established $Fe^{3+/2+}$ and $Fe^{2+/1+}$ charge transfer levels are summarized and predictions on the positions of further charge transfer levels are made based on the internal reference rule. The $Fe^{3+/4+}$ level has not been identified unambiguously in any of the studied materials. Detailed term schemes of the observed charge states in tetrahedral and trigonal crystal field symmetry are presented including hyperfine structure, isotope effects and Jahn–Teller effect. Particularly, the radiative transitions $Fe^{3+}(^4T_1 \rightarrow {}^6A_1)$ and $Fe^{2+}(^5E \rightarrow {}^5T_2)$ are analyzed in great detail.

An effective-mass-like state $[Fe^{2+}, h]$ consisting of a hole bound to Fe^{2+} is of great significance for a potential realization of spin-coupling in a DMS. New insights on this shallow acceptor state could be obtained by means of stress dependent and temperature dependent absorption experiments in the mK range. The binding energy and effective Bohr radius were determined for GaN, GaP, InP and GaAs and a weak exchange interaction between the hole and the Fe^{2+} center was detected.

With regard to the Fe^{3+} ground state, $^6A_1$, in GaP and InP, the hyperfine structure level Γ_8 was found to be above the Γ_7 level.

All results are discussed with respect to a potential realization of a ferromagnetic spin-coupling in DMSs.

1 Introduction

1.1 Application and motivation The Fe impurity in III–V and II–VI compound semi-conductors has been the subject of research for several decades. In the past, it was studied as an inevitable defect providing experimental information of interest for aspects of group theory. Fe is also introduced deliberately into semiconductor materials used in electronic and optoelectronic devices to achieve semi-insulating substrate material [1].

Today though, transition metal (TM) doped semiconductors are the major subject of recent attempts to realize ferromagnetic semiconductors for spintronics applications [2–9]. Such alloys represent dilute magnetic semiconductors (DMS). Potential mechanisms of a ferromagnetic coupling between the isolated TM ions are *superexchange*, *double-exchange* [10], *kinetic exchange* and an interaction involving bound magnetic polarons [4, 8]. In particular in the wide gap materials GaN and ZnO, a high potential to eventually achieve room temperature ferromagnetism through kinetic exchange in the form of hole mediated spin-coupling has been predicted (Zener model) [6]. Microscopically, the spin-coupling between the free carriers and the localized TM centers is established by exchange interaction. This approach requires high concentrations of TM ions and holes at the same time [6]. Also the charge state of the TM center is a critical parameter of the models mentioned above.

Many experimental and theoretical studies (mainly focussed on Mn) lack a comprehensive, quantitative understanding of the electronic structure of the TM centers. In

this paper, we summarize such experimental data of the Fe center in a wide range of III–V and II–VI host materials. Our goal is to provide crucial information required for an estimate of the feasibility of an Fe based DMS. We shall point out common phenomena that can be generalized to other TM's.

In order to gauge the potential of an Fe-doped semiconductor for a ferromagnetic coupling, the following questions need to be answered: (1) Which charge states of Fe are found and what states do they form within the band gap of the host material, especially near (~20 meV) the electronic bands? (2) What is the position of the charge transfer (donor or acceptor) levels? (3) Do we observe any type of interaction between the Fe center and itinerant carriers that might enable spin-coupling?

Those three questions are addressed in detail throughout this paper. On the basis of optical and magnetic studies, complete term schemes of Fe^{3+} (Section 3.2) and Fe^{2+} (Section 3.3) are established and the charge transfer energies are given as far as they are known (Section 2). Regarding the last question, we present new results on the shallow hydrogenic state consisting of a hole localized at Fe^{2+} (Section 4) that are significant in the context of spin-coupling via bound magnetic polarons [11].

2 Charge transfer levels In order to gauge the feasibility of an Fe based DMS it is most important to know the position of the charge transfer (CT) levels, i.e., donor and acceptor levels, formed by the Fe impurity.

2.1 Significance of charge transfer levels A transfer from one charge state of Fe into another can be established by transferring a d-electron from the Fe center into one of the bands of the host lattice or vice versa. The energy involved in this charge transfer process is the charge transfer energy and can be identified with a level within the band gap (see Fig. 1). The $Fe^{N/(N-1)}$ and $Fe^{N/(N+1)}$ levels represent deep acceptor $A^{0/-}$ and donor $D^{0/+}$ states, respectively. N is the charge state of the isoelectronic case. For Fe on cation site, N is 3+ and 2+ for III–V and II–VI compounds, respectively. The CT levels $Fe^{N/(N-1)}$ and $Fe^{N/(N+1)}$ are usually found above and below the middle of the band gap, respectively. However, their exact position also depends on the stability of the involved charge states. For instance, the high correlation energy of the stable d^5 configuration of Fe^{3+} shifts the $Fe^{3+/2+}$ level to higher and the $Fe^{3+/4+}$ level to lower energies (Fig. 1).

In general, there is only one charge state present at equilibrium conditions. Which one that is depends on the position of the Fermi level in relation to the CT levels (Fig. 1). In thermodynamic equilibrium, the position of the Fermi level is a function of donor and acceptor concentrations and therefore may again depend on the Fe concentration [12]. In the case of high Fe concentrations needed for the potential realization of a ferromagnetic semiconductor, the position of the Fermi level may be governed mainly by the Fe impurity. Consequently, two charge states could be present pinning the Fermi level to the respective CT level. As the $Fe^{3+/2+}$ CT level is found near the middle of the band gap in most materials, this effect is exploited by heavy Fe-doping for producing semi-insulating material that is needed as substrate for electronic and optoelectronic devices [1].

Other charge states may be created (activated) in non-equilibrium conditions. For instance, optical excitation may induce a charge transfer either directly in the form of a Fe *center to band* transition or by producing free carriers, i.e., shifting the Fermi level. Optically induced CT transitions starting from the isoelectric charge state are called photoionization, the ones terminating at it photo neutralization.

From the just discussed meaning of the position of the CT levels their significance in the context of ferromagnetic DMS's becomes apparent. The charge state and the resulting spin of the Fe center are crucial points when calculating a potential ferromagnetic coupling [8]. Hence, in order to make predictions on or achieve a particular charge state, the position of the CT levels needs to be known as precisely as possible. The donor and acceptor states formed by Fe may impede or support p- or n-doping. The promising approach of hole mediated spin-coupling requires high hole concentrations [6]. Here, the role of the TM center is decisive for a successful implementation. If the iron $A^{0/-}$ level is found close to or within the VB then the Fe center will not only provide localized spin but also the required holes. However, if the $D^{0/+}$ level is found within the band gap it will compensate the p-doping ($D^0 + h \rightarrow D^+$) by pinning the Fermi energy, unless it is located between the VB and the acceptor level of the p-dopant.

Enno Malguth is a Ph.D. student at the Institut für Festkörperphysik, Technische Universität Berlin and at the Microstructural Analysis Unit, University of Technology Sydney. His main field of research is the optical and magnetic characterization of transitional-metal-doped wide-band-gap semiconductors for potential spintronic applications. By the time of publication, he will have finished his Ph.D. and is starting a position as a postdoctoral fellow at the School of Electrical and Computer Engineering at the Georgia Institute of Technology where he wants to extend his research onto the growth of ferromagnetic semiconductors.

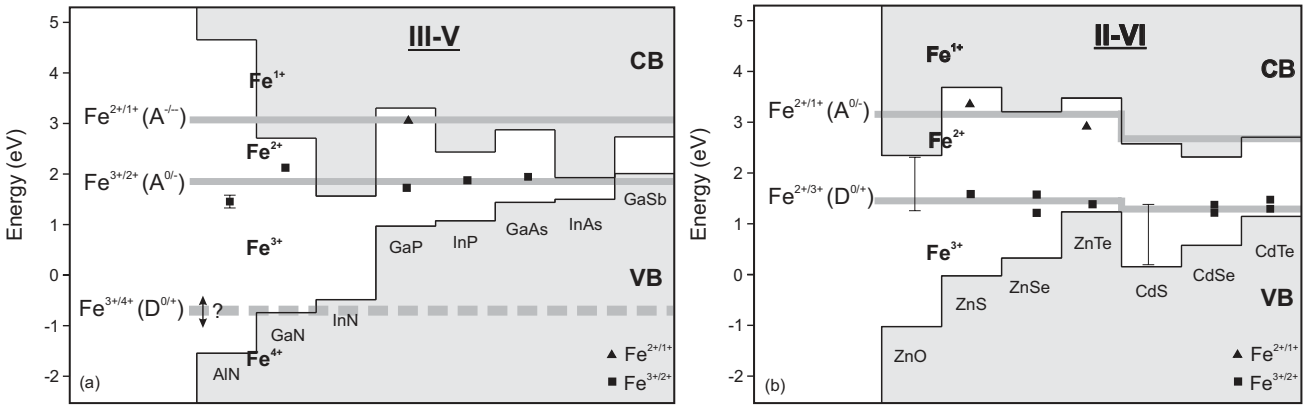

Figure 1 Charge transfer levels $Fe^{2+/1+}$, $Fe^{3+/2+}$ and $Fe^{3+/4+}$ in (a) III–V and (b) II–VI compounds. The band gaps and band off-sets were taken from [15, 16]. For recently established values of the band gap of InN, see Refs. [17, 18] and references therein. The CT values were taken from Table 1. Dark grey bars roughly indicate trends of common Fe levels according to the internal reference rule [13, 14]. They separate energy regimes of stable oxidation states. Regarding the II–VI materials (b), the potential trends are different for Zn and Cd compounds. The position of the $Fe^{3+/4+}$ level in III–V materials is still unclear.

Additionally, the position of the CT levels is also needed to place the term schemes of the single charge states that are established in Section 3 in the correct relation to the bands. It is also important regarding the internal reference rule that predicts band off-sets in semiconductor hetero-structures on the basis of TM CT levels [13, 14].

2.2 Determining the position of the CT levels

The position of the CT levels can be determined from observing the CT process (photoionization) in absorption, PL excitation, photo conductivity or photo ESR experiments where it appears as an exponentially rising band (see Figs. 2 and 9). The underlying processes were modeled successfully by Ridley et al. [19–21]. The low-energy onset of that band is the photoionization threshold and equals the distance between the CT level and the involved band. The values obtained this way are relatively inaccurate because the exact photoionization threshold is difficult to pinpoint. A more accurate method exploiting the effective-mass-like state [Fe^{2+}, h] is presented in Section 4.3.3.

Between two charge states, two CT processes can be observed in photoionization experiments:

$$Fe^{N} + h\nu_1 \rightarrow Fe^{N-1} + h_{VB}\,, \tag{1}$$

$$Fe^{N-1} + h\nu_2 \rightarrow Fe^{N} + e_{CB}\,. \tag{2}$$

Due to its s–d character transitions involving the s-like CB (Eq. (2)) have a much smaller oscillator strength and are more difficult to detect than those involving the p-like VB (Eq. (1)). In ZnS an energy transfer from one Fe^{2+} ion to another was observed in the form [22]

$$2Fe^{2+} + h\nu \rightarrow Fe^{3+} + e_{CB} + Fe^{2+} \rightarrow Fe^{3+} + Fe^{1+}\,. \tag{3}$$

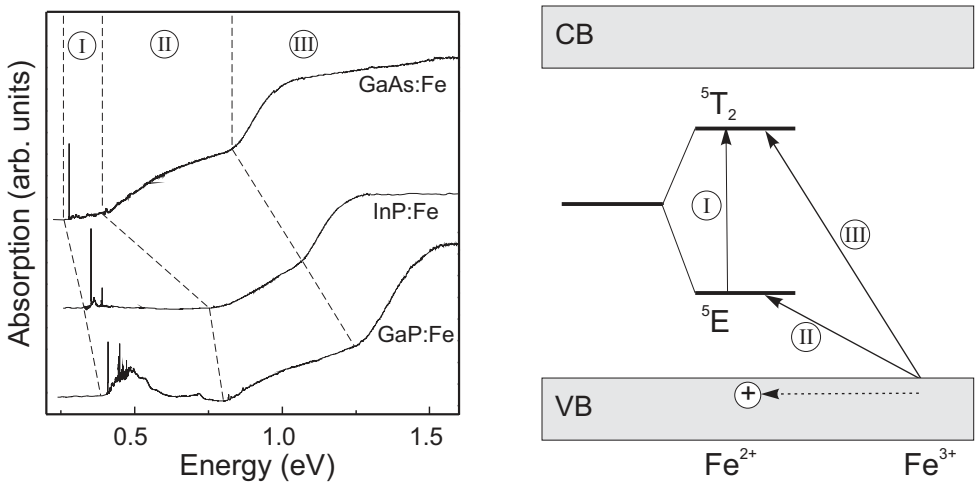

Figure 2 Typical absorption spectra of semi-insulating InP, GaAs and GaP. All spectra exhibit the internal $Fe^{2+}(^5E \rightarrow {}^5T_2)$ transition (I) and two charge transfer bands (II and III) representing $Fe^{3+} \rightarrow Fe^{2+}$ CT processes that result in the $Fe^{2+}(^5E)$ ground and $Fe^{2+}(^5T_2)$ excited state, respectively, while a hole is generated in the VB. The energy diagram on the right illustrates these three transitions.

It should be noted that, in general, the sum of the CT energies $h\nu_1$ and $h\nu_2$ (Eqs. (1) and (2)) does not equal the band gap energy because of lattice relaxation effects [23, 24]. In extreme cases these effects may be of magnitudes up to 0.3 eV [24]. Another issue of determining the CT level from photoionization spectra is that the observed CT process might be that of another defect and that the Fe charge state is simply changed by the free carriers created in that first process [12, 25].

The experimentally found CT levels are summarized in Table 1 and in Fig. 1. The CT process (Eq. (1)) terminating in both the ^5E and the $^5T_2$ states of Fe^{2+} has been observed in InP, GaAs, GaP and GaN (see Figs. 2 and 9) [12, 34]. Unfortunately, the $Fe^{3+/2+}$ level in ZnO has not been found to date although both charge states 3+ and 2+ have been observed [25, 35]. Here, the problem is that the holes that establish the CT process are generated via different defects at 2.25 eV [25]. While the $Fe^{2+/1+}$ level has only been observed in GaP and ZnS [26, 29] it must be found within the band gap of ZnSe, ZnTe and CdTe as well. In these materials both charge states Fe^{2+} and Fe^{1+} have been identified (Sections 3.3 and 3.4). Neither the $Fe^{3+} \leftrightarrow Fe^{4+}$ transition nor the Fe^{4+} state have been observed in any material to date. Merely theoretical calculations and tentative speculations based on near band edge luminescence put the $Fe^{3+/4+}$ level above the VB edge in GaN and AlN [36, 37].

From Fig. 1 further conclusions about so far unobserved CT levels can be drawn if we assume the band offsets to be correct and that the internal reference rule holds, i.e., that there is a trend in the position of the CT levels at least within related material systems. Among the III–V materials in Fig. 1(a) the only other material apart from GaP where the $Fe^{2+/1+}$ level can be expected to be found within the band gap is AlN. Regardless of the exact band gap energy of InN [17, 18], Fe^{3+} is probably the only stable charge state. Regarding the II–VI materials, if we distinguish between Zn and Cd compounds we get a better agreement with the internal reference rule for each group. From the respective trends we can conclude that if the $Fe^{2+/1+}$ level is really found within the band gap of ZnSe and CdTe it must be very close to the CB. In ZnO, the $Fe^{2+/1+}$ level is very likely to be found in the CB. The position of the $Fe^{3+/2+}$ level in ZnO can be narrowed down to be between 2.25 eV and 2.8 eV above the VB and in CdS to be between 1 eV and 1.3 eV.

Table 1 Experimentally determined position of the CT levels $Fe^{3+/2+}$ and $Fe^{2+/1+}$. The $Fe^{3+/4+}$ level has not been found in any material. The values are given in meV as measured from the VB maximum unless indicated otherwise. The values of GaP, InP and GaAs are derived in this work with high accuracy from a comparison of the binding energies of the bound state [Fe^{2+}, h] with effective mass theory (Section 4.3.3). The values of the other materials were determined from the photoionization threshold. Levels that have not been observed yet but that are believed to be found within the band gap because both charge states have been observed are labeled (gap).

material	$Fe^{3+/2+}$ (meV)	Ref.	$Fe^{2+/1+}$ (meV)	Ref.
GaP	851.8	[this work]	$E_{CB} - 240$	[26]
InP	800.6	[this work]		
GaAs	510.8	[this work]		
GaN	2870 ± 10	[12]		
AlN	3000 ± 300	[27]		
ZnS	$E_{CB} - 2100 \pm 100$	[28]	$E_{CB} - 240 \pm 100$	[29]
ZnSe	890, 1250	[13, 23]	(gap)	
ZnTe	$E_{CB} - 2240 \pm 50$	[30]	1700 ± 50	[30]
ZnO	>2250	[25]		
CdTe	350, 150	[31, 32]	(gap)	[30]
CdS	<1300	[33]		
CdSe	800, 640	[13, 23]		

2.3 Implications of the found charge transfer levels From the found position of the CT levels we can conclude that the $Fe^{3+/2+}$ acceptor level in GaN is too deep to act as a hole source in a potential DMS based on hole mediated spin-coupling. Here, additional p-doping would be required. However, as discussed above, if the $Fe^{3+/4+}$ donor level turns out to be found higher than a few tens of meV above the VB it will compensate the p-doping impeding the realization of hole-mediated ferromagnetism. This problem is quite likely to occur in AlN (see Fig. 1). The same applies for the II–VI materials included in Fig. 1 because the $Fe^{3+/2+}$ donor level is high above the VB in all of them. On the other hand, apart from GaN and AlN, the $Fe^{3+/4+}$ donor level is located well within the VB of III–V materials enabling p-doping. The only material included in Fig. 1 where Fe might act as a shallow acceptor is GaSb.

In intrinsic GaN where natural defects act as donors rising the Fermi level, iron is predominantly found in the Fe^{2+} charge state. At high Fe concentrations with the Fermi level pinned to the $Fe^{3+/2+}$ level both charge states are present and GaN becomes semi-insulating [12]. A similar behavior is expected for most other materials with intrinsic defects acting as donors.

Regarding the validity of the internal reference rule [13, 14], it can be concluded that it holds to a certain extend inside the three material groups Zn compounds, Cd compounds and phosphides/arsenides (see Fig. 1). Inside the nitrides and between these material groups it only provides a rough trend.

3 Electronic structure of the Fe charge states

The electronic structure of the different charge states of Fe occurring in III–V and II–VI semiconductors needs to be understood in order to make predictions about a potential spin-coupling.

Carrier mediated spin-coupling requires free carriers to interact with the Fe centers [6]. Therefore, levels close to the bands are of particular interest which free carriers could be captured in and released from at room temperature.

Another mechanism of ferromagnetic coupling, *double exchange*, is established by d-electrons hopping between

two isolated TM centers with different numbers of electrons [4, 8, 10, 38]. At large TM concentrations, partly filled itinerant impurity bands may be formed from Fe d-levels in the band gap. Both ferromagnetic coupling and electrical conduction are accomplished by hopping within these bands. No free VB or CB carriers are involved in double exchange. A good understanding of the electronic structure of all occurring Fe charge states is required for predictions about d-states potentially involved in that hopping process and the formation of such bands. Also the coupling mechanism involving *bound magnetic polarons* depends crucially on the configuration of the magnetic centers [39].

As discussed above, the charge state of the Fe center is a critical parameter in the models of carrier mediated spin-coupling. When applying optical and magnetic (e.g., electron spin resonance (ESR)) techniques to determine the present charge state of a new alloy containing Fe, a deep understanding of the electronic structures of potential charge states is essential to interpret the respective results.

In this section, we do not confine ourselves to the mere aspects of the electronic structure that are of interest for spin-coupling. Moreover, complete term schemes are presented including hyperfine structure, isotope effects and Jahn–Teller effect.

3.1 The emergence of the electronic structure

Incorporated into the host crystal the electronic structure of the Fe center is the result of a multiple splitting of the highly degenerate states of the free ion by symmetry reduction (Figs. 3 and 10). The Stark effect of the crystal field has the strongest impact. The resulting electronic structure can be approximated by the Hamiltonian

$$H = H_{\text{free ion}} + H_{\text{CF}} + H_{\text{SO}} + H_{\text{v}} + H_{\text{JT}}(+H_{\text{pert}}), \qquad (4)$$

with the perturbation terms: $H_{\text{free ion}}$ = Hamiltonian of free ion including multi electron interaction according to Hund's rule, H_{CF} = crystal field (Stark effect), H_{SO} = spin-orbit interaction, H_{v} = vibrational contributions, H_{JT} = electron–phonon coupling namely Jahn–Teller coupling, H_{pert} = possible further perturbation, e.g., axial distortion of the crystal field in hexagonal crystals (C_{3V} symmetry). Specific term schemes of Fe^{3+} and Fe^{2+} illustrating the various splitting processes are shown in Figs. 3 and 10, respectively.

III–V and II–VI materials predominantly crystalize in the cubic zincblende and the hexagonal wurtzite structure. Fe has been found to be preferably incorporated on the cation site which has a tetrahedral (T_d) symmetry in cubic crystals and a trigonal symmetry (C_{3V}) in hexagonal ones [40–42]. The trigonal case can be treated as a perturbation of the tetrahedron in the form of a slight axial distortion along the *c*-axis. The amplitude of the crystal field splitting is given by the crystal field parameter *Dq* and the spin–orbit splitting by the spin–orbit-coupling parameter λ. In this paper, Mullikan notation is used for the irreducible representation of crystal field states while Bethe notation is used for spin–orbit and less degenerate states.

The Fe center may suffer a Jahn–Teller effect, i.e., a spontaneous symmetry reduction by a displacement of the surrounding nuclei leading to a partial lift of degeneracy and a decreased over-all energy [43]. The energy difference between the symmetric and the distorted configuration is the Jahn–Teller energy (E_{JT}). As there are usually several such distorted configurations the system oscillates between them enabling a coupling to the vibrational motion of the lattice. This is called a dynamical Jahn–Teller effect and has a crucial impact on the electronic fine structure of the Fe center. Here, E_{JT} is a measure of the strength of the coupling to vibrational modes.

The eventual electronic structure can be determined experimentally by means of optical and magnetic experiments. The position of the term schemes within the band gap, i.e., the relation to the bands, infers from the the respective CT level which equals the position of the ground state.

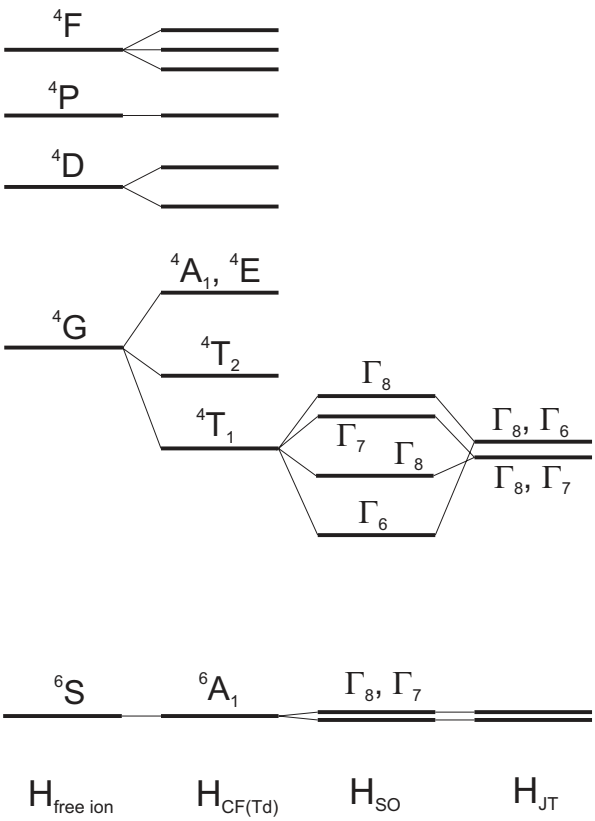

Figure 3 Qualitative term scheme of the Fe^{3+} center in a tetrahedral crystal field. The hamiltonian of the isolated ion and terms for the crystal field, spin–orbit interaction and Jahn–Teller effect are given at the bottom. The case of a trigonal crystal field of a hexagonal lattice is outlined in Fig. 8. The energetic differences are not to scale.

3.2 The Fe^{3+} center Fe^{3+} has a $3d^5$ configuration. Consequently, the free ion has a ^6S ground state and a ^4G first excited state (see Fig. 3). Under the impact of the T_d crystal field, the first transforms into a $^6A_1$ state and the latter splits into four states of $^4T_1$, $^4T_2$, ^4E and $^4A_1$ symmetry, in order of rising energy. Compared to the free ion, the energy difference between the crystal field states is reduced by the partially covalent bonding. The crystal field states are further split by spin–orbit coupling. The $^4T_1$ state splits into four states of Γ_6, Γ_8, Γ_7 and Γ_8 symmetry. The $^6A_1$ ground state is split neither by the crystal field nor by the spin–orbit coupling because of its singlet character. Only spin–spin interaction and second order spin–orbit terms lead to a splitting of a few μeV, into a Γ_8 and a Γ_7 state the energetic order of which is elucidated in Section 4.3.3. Beyond spin–orbit coupling, the Fe^{3+} states are also affected by symmetry reduction such as the axial distortion of the crystal field of hexagonal crystals and the Jahn–Teller effect. Since Mn^{2+} and Cr^+ also have d^5 configuration these ions exhibit a similar splitting and similar luminescence spectra. Excited states higher than $Fe^{3+}(^4T_1)$ have only been observed for GaN [12] meaning that in other materials these states are not found within the band gap or that they are degenerate with other electronic states.

3.2.1 The $(^4T_1 \rightarrow {}^6A_1)$ luminescence The only luminescent intra-center transition of Fe^{3+} is the 'spin-flip' $(^4T_1 \rightarrow {}^6A_1)$ transition. So far, it has been reported for GaAs [48], InP [46], GaN [12, 41, 50], ZnO [25] and ZnS [45]. This transition is forbidden by symmetry and spin selection rules. The electric dipole transition becomes allowed mainly by the admixture of odd-parity states of the ligands to the d-like TM states by the covalent bonding or the spin–orbit interaction with the ligands [51]. Figure 4 exemplifies the photo luminescence spectrum of that transition for GaN. Details derived from the observed $(^4T_1 \rightarrow {}^6A_1)$ luminescence are compiled in Table 2. Since the $(^4T_1 \rightarrow {}^6A_1)$ transition is forbidden by selection rules, it exhibits lifetimes in the ms range. Obviously there are no non-radiative relaxation processes between the two levels. The lifetimes decrease with rising degrees of covalency of the host crystal (order: ZnO, GaN, ZnS, (InP,GaAs)) because the $(^4T_1 \rightarrow {}^6A_1)$ transition is made allowed by the covalent part of the bonding [51, 52]. Covalency also reduces the energy difference $^4G - {}^6S$ of the free ion of 4.07 eV [53]. Hence, also the energy of the $(^4T_1 \rightarrow {}^6A_1)$ transition decreases with the covalency of the crystals in the same order (Table 2).

In Fig. 4, a pronounced phonon sideband can be seen which is quite similar for all studied host materials. Detailed analyses of the sideband can be found in Refs. [12, 25, 45, 46, 48]. In brief, most replica can be attributed to replicas of LO and TO phonons at the center of the Brillouin zone as well as to defect specific vibrational modes. Particularly, a strong coupling on E_2 modes is common for all host materials. It will be discussed below in the framework of the Jahn–Teller effect. Defect specific vibrational modes are discussed in more detail in Section 5. Multiple zero phonon lines in ZnO and ZnS are accounted for by an isotope effect (Section 3.2.2) and by the polymorphic

Table 2 Observations on the $Fe^{3+}(^4T_1 \rightarrow {}^6A_1)$ luminescence. Energy, FWHM, lifetime as well as the fine structure of the involved states are listed for various host materials. The fine structure of the $^6A_1$ state was resolved by interpolating the zero field splitting in Zeeman measurements. More detailed information on the $^6A_1$ fine structure obtained from magnetic experiments is given in Table 3. All values are given for liquid helium temperature. Concerning the host materials listed in the first column, c and h refer to the cubic (T_d) and hexagonal (C_{3V}) lattice structure, respectively. The labeling of ZnS polytypes (AN, PN, AS, PS) refers to the notation of Buch et al. [44]. Where several kinds of one polytype were observed, the values of the most prominent line are given [45]. Fe in AlN has only been studied very roughly [27].

host	energy	FWHM	lifetime	excited state $^4T_1$		ground state $^6A_1$	
material	(eV)	(μeV)	(ms)	assignment of sublevels	splitting (meV)	assignment of sublevels	splitting (μeV)
GaP c	not observed						
InP[a] c	0.5331	32	1.1	Γ_7, Γ_8, $\Gamma_{6,8}$	0.51, 2.73		
GaAs[b] c	0.3790	≈100	1.9	Γ_7, Γ_8, $\Gamma_{6,8}$	0.74, 1.61		
GaN[c] h	1.2990	120	8.0	Γ_4, $\Gamma_{5,6}$, Γ_4, $\Gamma_{4,5,6}$, Γ_4	1.10, 1.72, 2.42, 3.65	$\Gamma_4(\pm5/2)$, $\Gamma_{5,6}(\pm3/2)$, $\Gamma_4(\pm1/2)$	38, 59
AlN[d]	1.297		4.5				
ZnO[e] h	1.7874	48	25.2	Γ_4, $\Gamma_{5,6}$, Γ_4, Γ_4, $\Gamma_{4,5,6}$	1.20, 1.34, 2.62, 4.4	$\Gamma_4(\pm5/2)$, $\Gamma_{5,6}(\pm3/2)$, $\Gamma_4(\pm1/2)$	33, 43
ZnS[f] c (AN)	1.0140	180	4.3	$\Gamma_{7,8}$, $\Gamma_{6,8}$	0.58		
ZnS[f] (PN)	1.0182	300	3.3	four (unassigned)	0.86, 1.72, 2.75		
ZnS[f] (AS)	1.0256	250	3.1	$\Gamma_{7,8}$, $\Gamma_{6,8}$	0.48[g]		
ZnS h (PS)		not observed					

[a] [46, 47], [b] [48, 47], [c] [12, 49], [d] [27], [e] [25], [f] [45]

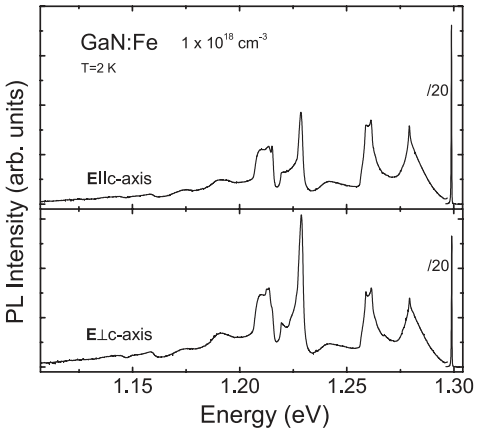

Figure 4 Polarized photo luminescence spectra of the Fe^{3+}($^4T_1 \rightarrow {}^6A_1$) transition in GaN. Very similar phonon sidebands are found for the same transition in other host materials.

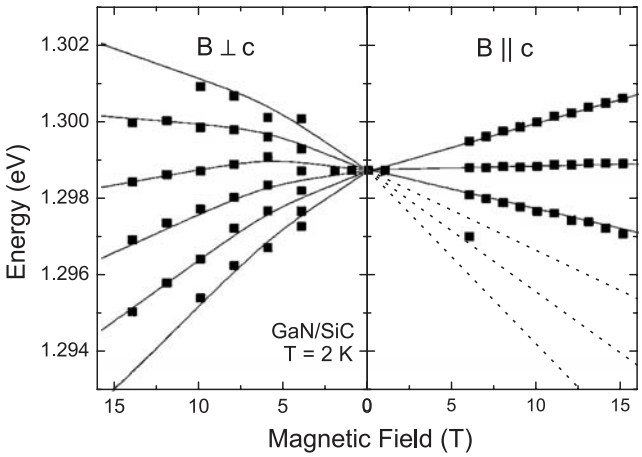

Figure 5 Zeeman behavior of the ($^4T_1 \rightarrow {}^6A_1$) luminescence in GaN. Since the spectra were recorded at $T = 2$ K they show the splitting of the $^6A_1$ ground state. The lines represent fits of the magnetic behavior on the basis of Eq. (5).

host crystal, respectively [25, 45]. In GaN, additional ZPL's originating from defect complexes involving Fe^{3+} have been found [12, 54].

3.2.2 Isotope effect of the ($^4T_1 \rightarrow {}^6A_1$) luminescence For ZnO, an isotope shift of the ($^4T_1 \rightarrow {}^6A_1$) energy was reported by Heitz et al. [25]. A shift of +39 μeV/nucleon occurs due to the natural abundance of Fe isotopes. Also the replacement of one of the ^{16}O ions of the tetrahedral $Fe^{3+}O_4^{2-}$ cluster by ^{18}O causes a shift of 365 or 222 μeV depending on the position within the tetrahedron. The isotope effect can be explained sufficiently by the contribution of mass-dependent local vibrational modes to the total energy of the involved states. In this context, also the Jahn–Teller coupling on such modes as well as the distortion of the $Fe^{3+}O_4^{2-}$ cluster in the hexagonal lattice need to be taken into account [25].

3.2.3 The $^6A_1$ state Due to the absence of orbital momentum the $^6A_1$ state in T_d symmetry is only split by spin–spin and second order spin–orbit interaction into two states of Γ_7 and Γ_8 symmetry. Until today, the correct energetic order of the Γ_7 and Γ_8 states has been unknown. In Section 4.3.3 we present CAS data indicating that, in GaP and InP, the Γ_8 level is above the Γ_7 level. The magnitude ΔE of this splitting is given by the fine structure constant a and $\Delta E = 3a$. In hexagonal crystals (C_{3V} symmetry), the axial distortion of the crystal field causes a split into three Kramers doublets with the $S_Z = \pm 3/2$ and $S_Z = \pm 1/2$ states a few tens of μeV above the the $S_Z = \pm 5/2$ ground state. This splitting is represented by the parameters D and F of the spin-Hamiltonian (see below). Further symmetry reduction may lead to an even stronger splitting. For example, in monoclinic symmetry resulting from Fe^{3+} associated with a monovalent point defect, a zero field splitting of the $^6A_1$ state of up to 630 μeV was observed by Holton et al. in II–VI materials [55].

The following spin-Hamiltonian describes the magnetic behavior of the $^6A_1$ state of a d^5 system ($S = 5/2$) and, thus, includes the just outlined fine structure for a magnetic field equal zero [56].

$$H = g\beta \cdot \boldsymbol{H} \cdot \boldsymbol{S} + \frac{a}{6}\left(S_\xi^4 + S_\eta^4 + S_\zeta^4 - \frac{707}{16}\right) + D\left(S_Z^2 - \frac{35}{12}\right) + \frac{7F}{36}\left(S_Z^4 - \frac{95}{14}S_Z^2 + \frac{81}{16}\right). \quad (5)$$

The axial symmetry component of a C_{3V} crystal field, given by the terms proportional to D and F, lies within the z-axis, the c-axis of a hexagonal lattice. This axis corresponds to a [111] axis in the cubic system given by ξ, η and ζ, in which the cubic part of the crystal field is defined by the fine structure constant a.

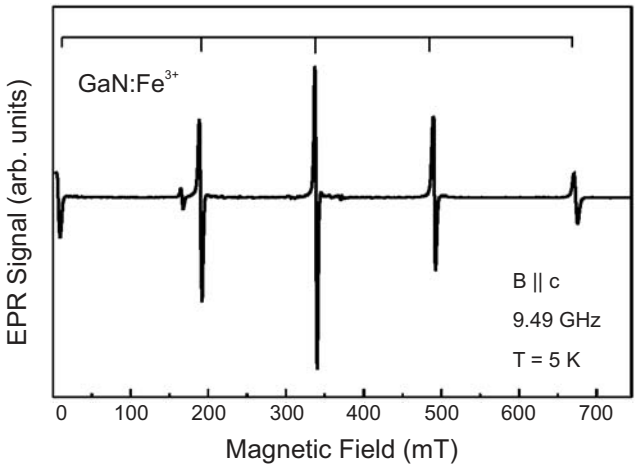

Figure 6 X-band (~9.5 GHz) ESR spectrum of Fe doped GaN with a Fe concentration of 1×10^{19} cm^{-3} at 5 K for $B \parallel c$-axis. The line positions of the five allowed fine-structure transitions ($\Delta M = \pm 1$) are indicated.

Table 3 Ligand field parameters for the spin-Hamiltonian of the $^6A_1$ state determined from Zeemann and ESR experiments. Concerning the host materials listed in the first column, c and h refer to the cubic (T_d) and hexagonal (C_{3V}) lattice structure, respectively. Only Fe centers of axial symmetry have values of D and F that are different from zero. Regarding ZnS axial polytypes, it is not clear which form of axial polytype was detected [44]. Where g is anisotropic, || and ⊥ refer to the direction with respect to the c-axis.

	D (μeV)	a (μeV)	a-F (μeV)	g	Ref.
ZnO h	–7.38	0.51	0.46	2.0062	[58, 59]
GaN h					
– on SiC	–9.32	0.60	0.65	$g_{\|}$ = 1.990, $g_{\perp}$ = 1.997	[49]
– on sapphire	–8.84	0.60	0.65	$g_{\|}$ = 1.990, $g_{\perp}$ = 1.997	[41]
– freestanding	–9.52	0.97	0.78	2.006	[42]
GaP c	–	4.85	–	2.026	[60]
GaAs c	–	4.22	–	2.046	[61]
InP c	–	2.74	–	2.0235	[62]
InAs c	–	5.22	–	2.035	[63]
ZnTe c	–	–32.40	–	2.0967	[64]
CdS h	–0.37	≈ 0.7		2.01	[65]
CdTe c		±23.6		2.084	[66]
ZnS AN c	–	1.58	–	2.0194, 2.026	[45, 57, 67]
ZnS (axial$_1$)	–5.95	1.57	1.65	$g_{\|}$ = same as AN polytype	[44]
ZnS (axial$_2$)	–5.70	1.57	2.31	$g_{\|}$ = same as AN polytype	[44]
ZnS PS h	not observed				

In a magnetic field, the $^6A_1$ state splits into six levels with $S_z = \pm 1/2, \pm 3/2$ and $\pm 5/2$. This splitting can be resolved in Zeeman and ESR experiments. Typical spectra are presented in Figs. 5 and 6, respectively, for Fe^{3+} in GaN. Zeeman spectra of the ($^4T_1 \rightarrow {}^6A_1$) luminescence obtained for ZnO, GaN and ZnS show that with increasing magnetic field the splitting is linear for $B \| c$ and nonlinear for $B \perp c$ (see Fig. 5). In both cases, the center of gravity shifts towards lower energies [25, 45, 49]. The five ESR resonances in Fig. 6 have been observed for any of the host lattices listed in Table 3. They represent transitions between the six Zeeman-split levels.

The values of the parameters representing the zero field splitting in various host materials were derived from such magnetic experiments. They are summarized in Table 3. The fine structure constant a is almost one order of magnitude smaller in axial symmetry than in tetrahedral symmetry.

The absence of orbital momentum leads to g-values close to that of the free electron. While mostly isotropic g-factors are reported in the literature, GaN epilayers exhibit a dependence on the orientation of the external magnetic field with respect to the c-axis [41, 49]. Strain induced by the hetero-substrate is probably responsible for this anisotropy. In ESR measurements on Fe doped cubic ZnS, Räuber and Schneider resolved an isotope effect [57]. They observed a splitting of the central fine structure line caused by the natural abundance (2.2%) of Fe^{57}.

3.2.4 The $^4T_1$ state The fine structure of the $^4T_1$ state as outlined in Fig. 3 cannot be studied by means of absorption measurements because of the small oscillator strength of the ($^6A_1 \rightarrow {}^4T_1$) transition. Instead, it has been resolved by temperature dependent PL experiments of the ($^4T_1 \rightarrow {}^6A_1$) transition (see Fig. 7). With increasing temperature "hot lines" appear on the high energy side of the original ZPL representing higher $^4T_1$ levels. The results are compiled in the fifth and sixth column of Table 2.

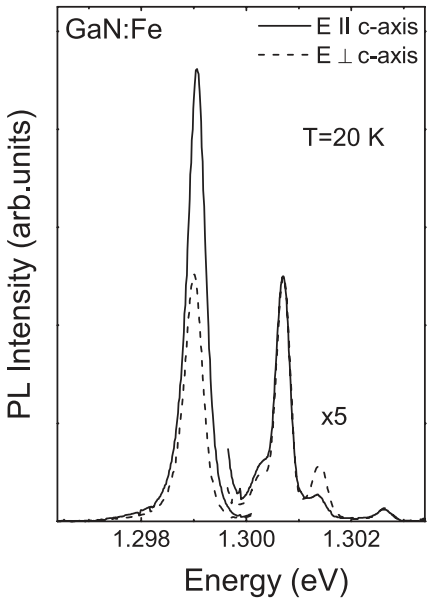

Figure 7 Polarized luminescence spectra of the Fe^{3+}($^4T_1 \rightarrow {}^6A_1$) transition in GaN excited at 2.41 eV at $T = 20$ K. With increasing temperature, higher $^4T_1$ sublevels are populated resulting in additional ZPL's on the high-energy side of the main peak.

As depicted in Fig. 3, according to static crystal field theory, the excited $Fe^{3+}(^4T_1)$ state is predicted to suffer a four fold splitting by spin–orbit interaction of roughly 10 meV. However, as can be seen in Table 2, in cubic II–VI and III–V semiconductors the four sub levels Γ_6, Γ_8, Γ_7, Γ_8 of the $^4T_1$ state are found to be reduced to a doublet or triplet with a splitting of only about 2 meV [45–48]. As illustrated in Fig. 3, the $^4T_1$ state is affected by a strong dynamic Jahn–Teller coupling to E-type phonon modes drastically reducing the orbital momentum [47, 68]. This phenomenon is even more pronounced for the $^4T_1$ state of tetrahedrally coordinated Mn^{2+} (isovalent with Fe^{3+}). Here, in the static limit, the Jahn–Teller effect fully quenches the first-order spin–orbit interaction leading to a characteristic doublet that can be explained by second-order spin–spin and spin–orbit interactions [68]. The observed fine structure lines of $Fe^{3+}(^4T_1)$ in cubic crystals could not be assigned unambiguously to particular $^4T_1$ sub levels [45–48].

In case of the trigonal symmetry of a hexagonal host crystal or axial polytype, the lower defect symmetry stabilizes the Fe^{3+} center against the Jahn–Teller coupling [12, 25, 45]. As a result, an only intermediate dynamic Jahn–Teller effect reduces the spin–orbit splitting to about 4 meV (Table 2). Additionally in C_{3V} symmetry, the four $^4T_1$ states are split into states of Γ_4, Γ_5, Γ_6 symmetry as outlined in Fig. 8. This splitting has only been resolved in hexagonal ZnO and GaN [12, 25]. Polarized measurements suggest that in GaN the top states Γ_7 and Γ_8 swap their energetic positions [12].

In summary, the fine structure of the $Fe^{3+}(^4T_1)$ state is the result of spin–orbit interaction, spin–spin interaction, the axial distortion in C_{3V} symmetry and a strong or intermediate Jahn–Teller effect in cubic and hexagonal crystals, respectively.

Only little is known about the magnetic behavior of the $^4T_1$ state. Merely a shift and twofold Zeeman splitting has been observed for the lowest state in hexagonal ZnO and GaN and the cubic polytype of ZnS [25, 45, 49]. Anisotropic g-factors were found for ZnO ($g_{\|} = -2.71$, $g_{\perp} = 0.27$) and GaN ($g_{\|} = -2.81$) [25, 49].

3.2.5 Higher excited Fe^{3+} states As mentioned above, higher excited Fe^{3+} states have only been observed in GaN [12, 69]. Figure 9 presents the PLE spectrum of the ($^4T_1 \rightarrow {}^6A_1$) luminescence in GaN. Transitions from the $^6A_1$ ground state into the excited states $^4T_2$ and ^4E appear at 2.0172 eV and 2.725 eV, respectively. Concerning the $^4T_2$ state, high-resolution spectra reveal a four fold splitting of about 10 meV with the lowest state at 2.0091 eV. In accordance with the $^4T_1$ state and in contrast to the Mn^{2+} center in cubic materials, the Jahn–Teller coupling is softened by the axial symmetry of the ligand field [68–71]. The high-energy sideband is the result of a dynamical Jahn–Teller effect on the vibronic levels of the $^4T_2$ state [69, 71].

The smallest FWHM found for the ($^6A_1$–^4E) peak is 7.4 meV. Since other measurements on the same sample suggest a relatively strain free incorporation of the Fe center, the mechanisms behind the relatively large value are still unclear. Two peaks separated by 1.4 meV were identified by means of polarized transmission experiments [12]. No assignment of the resolved sub-levels could be given for either state.

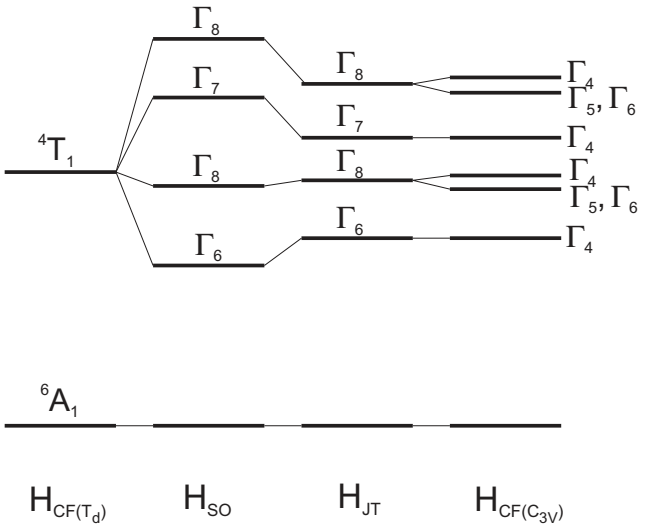

Figure 8 Energy scheme of the $Fe^{3+}(^4T_1)$ state in a C_{3V} crystal field. The spin–orbit splitting is not quenched as drastically by Jahn–Teller coupling as in T_d symmetry. Due to the axial distortion an additional splitting occurs into states of Γ_4, Γ_5 and Γ_6 symmetry. This fine splitting has been observed for ZnO and GaN [12, 25].

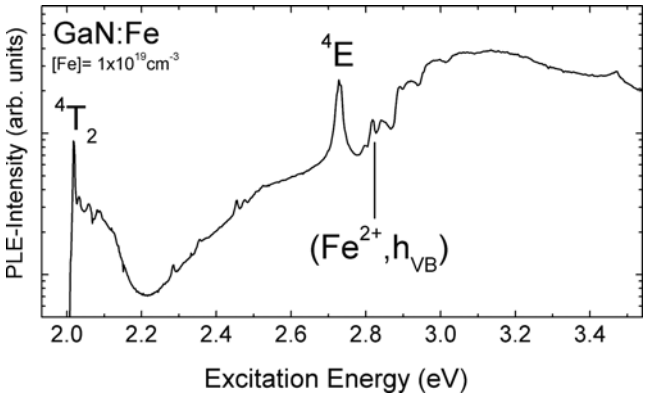

Figure 9 PLE spectrum of the ($^4T_1 \rightarrow {}^6A_1$) luminescence in GaN taken from Ref. [12]. Peaks at 2.0172 eV and 2.7247 eV represent transitions from the $^6A_1$ ground state into the excited states $^4T_2$ and ^4E, respectively. The broad band starting at 2.86 eV represents the charge transfer process $Fe^{3+} + h\nu \rightarrow Fe^{2+} + h_{VB}$ in which a hole is excited into the valence band. The small resonances at the onset of the charge transfer band represent a hydrogenic state where the valence band hole stays bound to Fe^{2+}. This state is dealt with in detail in Section 4. Phonon replica of the corresponding transition superimposed on the charge transfer band are responsible for the step-like structure. The broad band starting at about 2.2 eV represents the generation of free holes via native defects involved in the yellow luminescence of intrinsic GaN.

3.2.6 Excitation processes of the ($^4T_1 \rightarrow {}^6A_1$) luminescence In II–VI and III–V materials, two excitation processes of the ($^4T_1 \rightarrow {}^6A_1$) luminescence, i.e, mechanisms resulting in the $Fe^{3+}(^4T_1)$ state, have been found: intra-center excitation and the recombination of free holes with Fe^{2+}. Of course, intra-center excitation is only possible if iron is present in the 3+ charge state. The generation of free holes via a $Fe^{3+/2+}$ CT process and subsequent capture by Fe^{2+}

$$Fe^{3+}(^6A_1) + h\nu \rightarrow Fe^{2+} + h_{VB} \rightarrow Fe^{3+}(^4T_1), \quad (6)$$

has been observed for GaAs [72], GaP [73], InP [46], ZnS [45], ZnO [25] and GaN [12] in the form of broad CT bands (Fig. 9). Depending on the host material, the second part of Eq. (6) may be a multi-step process involving the bound state [Fe^{2+}, h] (Section 4) and higher excited Fe^{3+} states. Except for the ($^4T_1 \rightarrow {}^6A_1$) transition, all intra-center relaxation processes have been found to be non-radiative [12]. Also resonant excitation into the bound state represents an efficient excitation process in these materials as can be seen from PLE spectra, e.g., small resonances at 2.812 eV in Fig. 9. In ZnO, ZnS, and GaN, also defects other than iron act as additional hole sources. That is Cu^{2+} in ZnS [45], the defects responsible for the yellow luminescence in GaN (Fig. 9) [12], and unknown deep acceptors in ZnO with ionization energies above 2.25 eV [25]. Of course, a hole generation via band edge excitation works for all materials as well.

3.3 The Fe^{2+} center

3.3.1 Term scheme Fe^{2+} is difficult to detect by ESR because $3d^6$ is a non-Kramers configuration. Therefore, most of our knowledge about the electronic structure of the Fe^{2+} center in semiconductor materials is based on optical methods.

According to crystal field theory, the splitting of the ^5D ground state of the Fe^{2+} ion ($3d^6$, $L = 2$, $S = 2$) is described by the following Hamiltonian [79]:

$$H = H_{CF} + H_{SO} = B_4(O_4^0 + 5O_4^4) + \lambda \cdot \boldsymbol{L} \cdot \boldsymbol{S}, \quad (7)$$

with $B_4 = -Dq/12$ and the Stevens's equivalent operators O_4^0 and O_4^4. The ^5D state is split by the impact of the tetrahedral crystal field into a ^5E ground and $^5T_2$ excited state separated by $\Delta = 10\,|Dq| \sim 400$ meV (Fig. 10). As can be seen in Fig. 10, the former is split by spin–orbit interaction proportional to λ^2/Dq into five equidistant levels and the latter proportional to λ into six sates (λ = spin–orbit-coupling parameter) [79, 80]. However, it has been shown that crystal field theory alone cannot explain the experimentally observed fine structure. In fact, a dynamical Jahn–Teller coupling to E phonon modes defines the fine structure [78, 81]. Further splitting on account of symmetry reduction through axial distortion of the crystal field in hexagonal crystals or uniaxial pressure will be dealt with in the form of a perturbation of the tetrahedral crystal field in Sections 3.3.6 and 3.3.7, respectively.

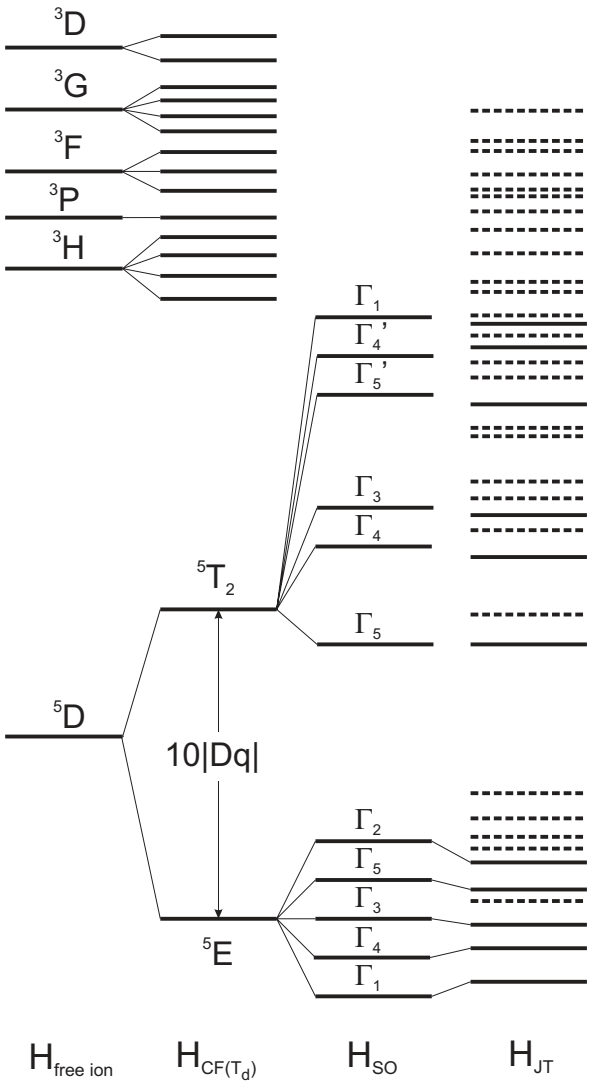

Figure 10 Qualitative term scheme of the Fe^{2+} center in a tetrahedral crystal field. The hamiltonian of the isolated ion and terms for the crystal field, spin–orbit interaction and Jahn–Teller effect are given at the bottom. The scheme is not to scale. The effects of the Jahn–Teller coupling (H_{JT}) are only adumbrated. The exact behavior depends on the host material and can be found in the respective Refs. [75–78]. In general, the Jahn–Teller effect causes vibrational levels to shift, split and mix. Dashed lines indicate levels arising from higher vibrational states. A term scheme illustrating further splitting in C_{3V} symmetry while ignoring the Jahn–Teller effect can be found in Fig. 13.

3.3.2 The ($^5E \rightarrow {}^5T_2$) transition In tetrahedral symmetry, the over-all optical transition ($^5E \rightarrow {}^5T_2$) is both electric- and magnetic-dipole-allowed [80]. Symmetry selection rules for individual transitions between spin–orbit levels of the ^5E and $^5T_2$ states are displayed in Table 4. The ($^5E \rightarrow {}^5T_2$) transition has been observed by absorption and luminescence experiments in ZnS [80–82], CdTe [80], GaN [83], GaAs [48, 72], GaP [84], InP [85–87], ZnO [35], ZnTe [77, 88], ZnSe [89, 90], CdS [90], CdSe

Table 4 Selection rules for otpical transitions in T_d symmetry. Allowed transitions are ticked.

T_d	Γ_1	Γ_2	Γ_3	Γ_4	Γ_5
Γ_1					✓
Γ_2				✓	
Γ_3				✓	✓
Γ_4		✓	✓	✓	✓
Γ_5	✓		✓	✓	✓

[91]. Exemplary transmission and PL spectra of the $Fe^{2+}({}^5E \rightarrow {}^5T_2)$ transition in ZnS and InP are shown in Figs. 2, 11 and 12. Table 5 summarizes the energy and the lifetime of the $({}^5E \rightarrow {}^5T_2)$ transition for various host materials. It also lists crystal field and spin–orbit splitting parameters determined from optical spectra using Hamiltonian 7. For almost all host materials the $({}^5E \rightarrow {}^5T_2)$ transition is found between 300 meV and 400 meV. The λ values have to be taken with care as they were determined neglecting Jahn–Teller effects. Except for CdTe, the values of λ are close to that of the free ion of 12.8 meV indicating relatively small degrees of covalency and weak Jahn–Teller coupling. At low temperatures ($T \approx 2$ K) where only the $\Gamma_1({}^5E)$ state is appreciably populated, only the two transitions terminating at $\Gamma_5({}^5T_2)$ levels should be observed in absorption spectra, according to Fig. 10 and selection rules (Table 4). However, most of the prominent lines in Fig. 11 cannot be interpreted coherently in terms of phonon replica. Instead, they are ZPLs arising through electron phonon coupling in the form of a dynamic Jahn–Teller effect from vibronic levels of ${}^5T_2$ [78]. This will be gone into in more detail in Section 3.3.5.

Besides, pronounced replica associated with TA, LA, TO, LO lattice phonons and Fe specific vibrational modes occur particularly in PL spectra.

Table 5 The $({}^5E \rightarrow {}^5T_2)$ transition and derived crystal field and spin–orbit coupling parameters Dq and λ for various cubic (c) and wurtzitic (h) host materials. Notation of ZnS polytypes according to Buch [44]. All values were determined at liquid helium temperature. The λ values have to be taken with care as they were determined neglecting Jahn–Teller effects.

	energy $(\Gamma_5({}^5T_2) - \Gamma_1({}^5E))$ (meV)	life time $\Gamma_5({}^5T_2)$ (μs)	λ (meV)	Dq (meV)
InP c	352.6[a]	10[a]	–10.74[b]	–37.66[b]
GaAs c	372.2[c]	8.5[c]	–11.20[c]	–39.75[c]
GaP c	414.4[d]	6.6[e]	–11.49[d]	–44.04[d]
ZnS (AN) c	365.5[f]	5.5[g]	–11.53[h]	–42.2[f], –43.4[j]
ZnS (PN)	350.8[j]			
ZnS (AS)	365.3[k]			
GaN h	393.3[l]			
ZnSe c	339.5[m]	18[g]		
CdTe c	282.9[f]		–8[f]	–30.7[f]
CdS h	317.9[k]			
CdSe h	294.5[n]		–11.6[o]	–31.6[o]
ZnTe c	308.7[p]			–33.4[p]
ZnO h	397.2[q]			

[a] [85], [b] [87], [c] [72], [d] [84], [e] [93], [f] [80], [g] [94], [h] [95], [i] [96], [j] [97], [k] [90], [l] [83], [m] [88], [n] [91], [o] [98], [p] [77], [q] [35]

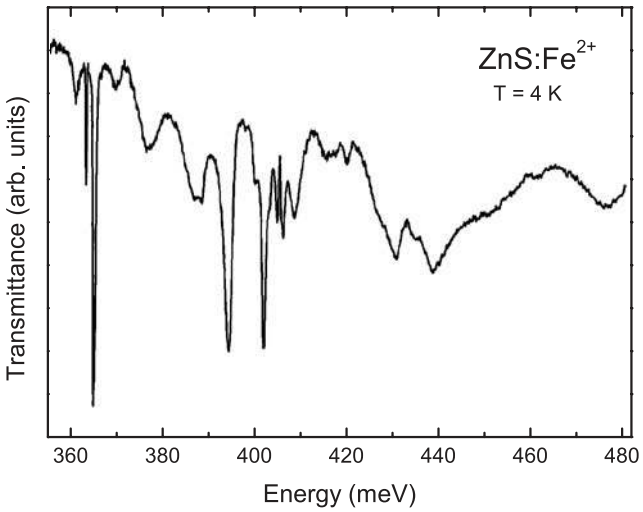

Figure 11 $Fe^{2+}({}^5E \rightarrow {}^5T_2)$ transition. Transmission spectrum of Fe-doped ZnS at $T = 4$ K. The common ground state of the present absorption lines is the $\Gamma_1({}^5E)$ state. The main ZPL represents the transition into the $\Gamma_5({}^5T_2)$ state which is unaffected by Jahn–Teller coupling. Lines at higher energies represent transitions into higher excited ${}^5T_2$ states that are the result of a strong Jahn–Teller coupling to TA and TO phonon modes. Taken from [78].

3.3.3 Isotope effect of the $Fe^{2+}({}^5E \rightarrow {}^5T_2)$ transition An isotope effect on the $({}^5E \rightarrow {}^5T_2)$ transition was observed on InP, GaP and GaAs in the form of a fourfold

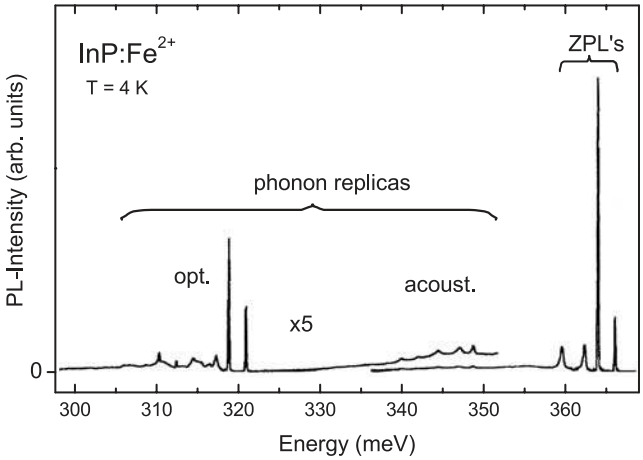

Figure 12 $Fe^{2+}({}^5E \rightarrow {}^5T_2)$ luminescence in InP at $T = 4$ K. The four ZPL's represent transitions from the $\Gamma_5({}^5T_2)$ state into the four bottom ${}^5E$ states (Fig. 10). The transition into the $\Gamma_2({}^5E)$ state is forbidden by selection rules (Table 4). Taken from [92].

fine structure of the ZPL's in absorption and PL spectra [72, 84, 85]. The relative intensities of these components agree with the natural abundance of the stable Fe isotopes ^{54}Fe, ^{56}Fe, ^{57}Fe and ^{58}Fe. The magnitude of the isotope shift is +19, +28 and 20 μeV/nucleon for InP, GaP and GaAs, respectively. The mechanisms behind isotope effects in optical spectra are outlined in Section 3.2.2.

3.3.4 The ^{5}E ground state Insights into the fine structure of the ^{5}E state are gained from infrared luminescence spectra of the $\Gamma_5(^5T_2) \rightarrow {}^5E$ transition [72, 77, 82, 84, 85, 87, 90, 91, 99, 100] as well as from far-infrared absorption spectra of transitions between ^{5}E sublevels [95, 101, 102]. The ^{5}E ground state was found to be almost sufficiently described by crystal field theory [80, 102]. It is not split by first order spin–orbit interaction. In second order it splits into five equally spaced levels separated by $\Delta E = 6\lambda^2/\Delta$ [79]. With equal values for $\lambda \approx 11$ meV in all materials (see Table 5), the distance between spin–orbit sublevels is roughly 1.9 meV. Third order perturbation terms cause only minor deviations from this homogenous splitting [103].

For small external magnetic fields, the Zeeman splitting of ^{5}E sublevels in cubic compounds is isotropic and can be explained by simple crystal field theory [102, 103]. If the magnetic field is strong and the Zeeman energy is of the magnitude of the spin–orbit coupling then Van Vleck paramagnetism arises leading to an anisotropic Zeeman behavior [103, 104]. Furthermore, in Zeeman measurements on Fe doped GaP and InP, a reduction of the orbital momentum by a factor of 0.2 was observed and assigned to a dynamic Jahn–Teller effect [92, 103].

Additionally, a weak dynamic Jahn–Teller coupling to *E* phonon modes at the edge of the Brillouin zone was found to shift, split and mix vibrational levels of the spin–orbit states [75–77, 106]. The Jahn–Teller coupling of the ^{5}E state is small in comparison to the spin–orbit coupling. As a consequence, transitions into vibronic states involving one or more vibronic quanta have small oscillator strengths and cause only weak peaks. Another consequence of the weak Jahn–Teller effect is that only small deviations from the fine structure predicted by plain crystal-filed theory occur in experiments. This is particularly true for host materials with large phonon energies that the Jahn–Teller effect is coupling to (e.g., III–V compounds, ZnS, ZnSe). In this case, first and higher vibronic states do not mingle but stay above zero phonon levels and only appear as low-energy bands in $\Gamma_5(^5T_2) \rightarrow {}^5E$ luminescence spectra [72, 75, 77, 82, 84, 85, 87, 90, 91, 99]. In case of small phonon energies (e.g., CdTe, ZnTe), higher vibrational states end up among the zero phonon levels causing additional luminescence lines [76, 77].

The Jahn–Teller effect was modeled successfully by adding a Jahn–Teller term to the Hamiltonian introducing a linear coupling [75–77, 106]. The resulting Jahn–Teller energies that are a measure of the magnitude of the coupling are compiled in Table 6. Also listed in Table 6 are the energies $\hbar\omega$ of the E-type modes that are involved in the Jahn–Teller coupling. These were found to be TA (L) phonons [75]. The calculated and experimentally confirmed fine structure of the ^{5}E state can be found in the references given in the first column of Table 6. Vogel et al. also calculated the ^{5}E fine structure for GaSb, InAs and GaSb for which no experimental data exist [75]. Similarities between the materials of Table 6 can be expected to also hold for all host crystals listed in Table 5.

Table 6 TA(L) phonon energies $\hbar\omega$ and Jahn–Teller energies E_{JT} used to model the $Fe^{2+}(^5E)$ fine structure in various host materials. The exact fine structure of the ^{5}E state can be found in the given references.

	$\hbar\omega$ TA(L) (meV)	E_{JT} (meV)
GaP[a]	10.3	1.0
GaAs[a]	7.7	1.0
InP[a]	6.8	0.9
GaSb[a]	5.7	1.0
InAs[a]	5.5	1.0
InSb[a]	4.1	1.0
ZnS[b]		0.9
CdTe[c]	3.7	0.35
ZnTe[d]	5.0	0.35

[a] [73], [b] [105], [c] [76], [d] [77]

The determined Jahn–Teller energies (≈1 meV) are relatively small confirming the Jahn–Teller coupling to be weak. While the spin–orbit splitting is hardly reduced the equal distances between the ^{5}E spin–orbit states are slightly altered [75].

Generalizing results on the $^5T_2$ state (Section 3.3.5), the ^{5}E state might also couple to optical phonons. However, given the relatively weak Jahn–Teller interaction found for ^{5}E this coupling is probably negligible.

3.3.5 The $^5T_2$ excited state According to crystal field theory, the $^5T_2$ state is split linearly in λ by first and second order spin–orbit coupling into six sates Γ_5, Γ_4, Γ_3, Γ_5', Γ_4', Γ_1 (Fig. 10) [79]. However, a dynamic Jahn–Teller effect with a magnitude comparable with that of the spin–orbit coupling needs to be considered in order to explain the final energy levels of $^5T_2$ as inferred from experiments [78, 81]. The vibronic coupling causes vibrational levels to shift, split and mix potentially producing a variety of ZPL's. Numerous studies have been performed to interpret absorption and luminescence spectra of the $Fe^{3+}(^5E \rightarrow {}^5T_2)$ transition in terms of a Jahn–Teller coupling to E-type lattice phonon modes [75, 80, 81, 106–112]. The most comprehensive, consistent and recent one was done by Mualin, Vogel and coworkers [78]. As previously proposed [81], they considered a simultaneous coupling to transversal acoustical (TA1 (K)) and transversal optical modes at the edge of the Brillouin Zone and calculated the resulting Jahn–Teller effect by the Lanczos method. The parameters determined that way, namely

Jahn–Teller energies ($E_{JT} \approx 25$ meV) and the energies of the coupling phonons, are listed in Table 2 of Ref. [78]. While, particularly for II–VI compounds, the coupling to acoustical modes is stronger the coupling to optical phonons becomes more significant in III–V compounds. Similar Jahn–Teller energies within these groups indicate that the vibronic coupling is primarily related to the impurity ion and its surrounding symmetry. The only level unaffected by the Jahn–Teller coupling is the bottom Γ_5 state. Any higher $^5T_2$ level is the result of shifted, split and mixed vibronic levels involving acoustical and/or optical phonons. These $^5T_2$ fine structure levels are scattered over a range of ~30 meV and ~50 meV for II–VI and III–V compounds, respectively [78].

The experimentally and theoretically determined fine structures of the $^5T_2$ state resulting from Jahn–Teller effects in CdTe, ZnTe, ZnSe, ZnS, GaAs, InP, GaP are summarized in Tables 1 and 2 of Ref. [78], respectively, and Tables 1 and 2 of Ref. [111], respectively. The most complete knowledge has been obtained about the $^5T_2$ substates into which transitions from the $\Gamma_1(^5E)$ ground state are allowed. Only for these levels, there are sufficient experimental data as a basis for theoretical calculations. Similar to the ^5E state, in host materials with small TA phonon energies at the edge of the Brillouin Zone (e.g., CdTe), numerous levels result from higher vibronic states.

In previous works, the shift of vibronic levels had not been considered to the extend required to account for all features observed in absorption and luminescence spectra. Instead, most ZPLs were associated with vibronic replica and a partially quenched spin–orbit coupling [48, 72, 80, 81, 84, 85]. Previously found phenomena such as allegedly swapped energetic positions of spin–orbit states [72, 80, 84] can now be considered as misinterpretations made before the significant effects of Jahn–Teller coupling were calculated by Mualin, Vogel et al. [78].

In Zeeman experiments, the $\Gamma_5(^5T_2)$ state in GaP which is unaffected by Jahn–Teller coupling was found to split linearly into three components Γ_3, Γ_2, Γ_4 [103].

3.3.6 The Fe^{2+} center in C_{3V} symmetry In C_{3V} site-symmetry of hexagonal crystals, the axial distortion of the tetrahedron along the *c*-axis can be treated as a perturbation of the Hamiltonian 7 [113]. Figure 13 illustrates the resulting splitting. Detailed corrections resulting from the perturbation term $H_{C_{3V}}$ were calculated theoretically and can be found in Tables 7 and 8 of Ref. [113] for the ^5E and $^5T_2$ states, respectively. Γ_5 and Γ_4 spin–orbit levels split into pairs (Γ_1, Γ_3) and (Γ_2, Γ_3), respectively. The correct order cannot be predicted theoretically. The order presented in Fig. 13 was chosen to agree with experimental data [83, 90, 91, 98]. Selection rules for spontaneous and stimulated transitions between the resulting states also include the polarization of the light with respect to the *c*-axis (Table 7).

Table 7 Selection rules for electronic dipole transitions in C_{3V}-symmetry. Transitions marked '||' are allowed for $\boldsymbol{E} \parallel c$-axis, the ones marked '⊥' for $\boldsymbol{E} \perp c$-axis. Blank boxes stand for forbidden transitions.

C_{3V}	Γ_1	Γ_2	Γ_3
Γ_1	$\parallel$		$\perp$
Γ_2		$\parallel$	$\perp$
Γ_3	$\perp$	$\perp$	$\parallel/\perp$

So far, the simultaneous effects of C_{3V} symmetry and Jahn–Teller effect have only been investigated for the $^5T_2$ states [114]. Considering coupling to only one TA phonon, phonon energies and Jahn–Teller energies similar to zinc-blende compounds (Section 3.3.5) were found. Consequently, the Jahn–Teller coupling of the $Fe^{2+}(^5T_2)$ state is not quenched in C_{3V} symmetry as was found for the Fe^{3+} states (Section 3.2).

In optical studies on hexagonal GaN, CdSe, CdTe, CdS and axial polytypes of ZnS, a trigonal splitting complying with Fig. 13 was observed with magnitudes roughly around 1 meV for both ^5E and $^5T_2$ states [83, 90, 91, 98].

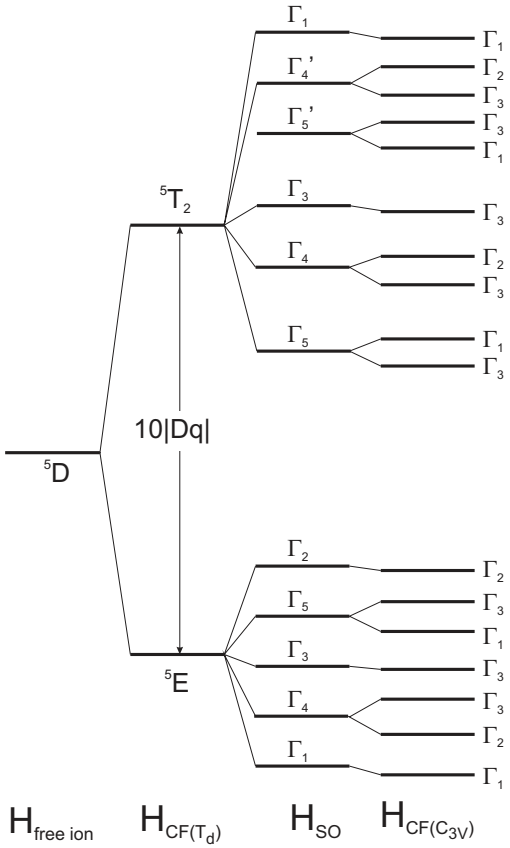

Figure 13 Theoretical splitting of the ^5E and $^5T_2$ states in C_{3V} symmetry ignoring the Jahn–Teller effect. The C_{3V} site-symmetry is treated as a perturbation of the tetrahedral crystal field. The order of the resulting states cannot be predicted. It was adjusted in accordance with experimental findings.

3.3.7 The Fe^{2+} center under uniaxial pressure The results of PL and absorption studies of the ($^5E \rightarrow {}^5T_2$) transition in cubic III–V semiconductors under uniaxial pressure comply well with group theory confirming the incorporation of Fe on cation-cite of perfectly tetrahedral symmetry [87, 103]. The impact of uniaxial stress is modeled in the form of a perturbation of the Hamiltonian 7. For stress parallel to the [111] direction, the site-symmetry becomes C_{3V} with the resulting splitting outlined above. However, in uniaxial stress experiments the splitting of the ^5E state has not been observed what is attributed to a dynamical Jahn–Teller effect [87]. For stress parallel to the [100] direction, the crystal field transforms into D_{2d} symmetry and Γ_3, Γ_4, Γ_5 states split into pairs of (Γ_1, Γ_3), (Γ_5, Γ_2) and (Γ_5, Γ_4), respectively. For stress along the [110] direction, the site-symmetry becomes C_S, all degeneracy is lifted completely and Γ_3, Γ_4, Γ_5 states split into states of Γ_1 and Γ_2 symmetry. For allowed transitions, the polarization of the light with respect to the direction of the applied stress depends on the symmetry of the involved states. Additionally, a shift of the distance ($\Gamma_5(^5T_2)$–^5E) to higher energies occurs [87, 103].

3.3.8 Higher excited Fe^{2+} states Figure 10 shows higher excited states of the free Fe^{2+} ion. Their energetic position is described by the Racah parameters. Crystal field states originating from these higher excited levels in tetrahedral symmetry have been observed by optical experiments on ZnS and ZnSe in the following energetic order: $^3T_1$, ^3E, $^3T_2$, $^3T_1$, $^3A_2$, $^3A_1$, $^3T_1$, $^3T_2$ [23, 90, 96, 115–117]. From those observations the Racah parameters were determined [96]. According to the position of the $Fe^{3+/2+}$ level in relation to the CB (Fig. 1(b)), higher excited Fe^{2+} states should be found inside the band gap of ZnTe as well.

3.4 The Fe^{1+} center Fe in the charge state 1+ ($3d^7$, $S = 3/2$) has been identified in GaP, ZnS, ZnTe, ZnSe and CdTe by means of optical studies and ESR [22, 29, 30, 118–120]. For the $^4A_2$ ground state, g-factors of 2.133, 2.251, 2.280 have been found in GaP, ZnS and ZnTe, respectively [22, 30, 118]. Intra-center transitions involving the ground state have been observed in ZnTe and ZnS at 0.967 eV and ≈0.8 eV, respectively [29, 30]. While the involved excited state is $^4T_2$ in ZnS it is uncertain in ZnTe.

The exact position of the established electronic Fe states in relation to the bands can be determined by putting together the CT levels (Section 2) with the term-schemes presented in the previous sections. However, no levels close (a few tens of meV) to one of the bands that are of particular interest for carrier mediated spin-coupling can be identified. Only in ZnS and ZnSe, the $Fe^{3+/2+}$ level is so deep in the band gap that the wealth of higher excited Fe^{2+} states (Section 3.3.8) is found in proximity to the CB. The found excited Fe^{1+} states are even located inside the CB. However, transitions between these states an the CB have small oscillator strength due to their s–d character rendering them uninteresting for carrier mediated spin-coupling.

Still, the thorough understanding of Fe centers obtained in this section is of significance regarding the pursuit of ferromagnetic spin-coupling. When studying new Fe doped alloys this knowledge will help determining the present charge state and aligning the results of optical and magnetic experiments.

4 The (Fe^{2+}, h) bound state A bound state consisting of a carrier localized at a non-isoelectric TM center holds significance regarding spin-coupling in DMS. In the III–V semiconductors GaP, InP, GaAs and GaN, such a hydrogenic state [Fe^{2+}, h] has been identified consisting of an Fe^{2+} ion (−1 with respect to the lattice) and a hole attracted by Coulomb interaction [12, 73, 121–126]. It can approximately be described by effective mass theory [127, 128] and represents a transient shallow acceptor state. This kind of effective-mass-like state has been observed in the following material systems as well: II–VI:Ni [129, 130], II–VI:Cu [131, 132], III–V:Co and III–V:Ni [133].

4.1 Significance of the [Fe^{2+}, h] state With its large Bohr radius this shallow acceptor state has a large capturing cross section [134, 135] significantly influencing the electrical and optical properties of the crystal.

Regarding spin-coupling in a DMS, this bound state (i.e., a bound magnetic polaron) holds various potentials depending on the TM concentration [4, 8]. At low concentrations, the average distance between the isolated TM centers is much larger than the effective Bohr radius. In this diluted regime, carrier mediated spin-coupling could be realized via holes being captured and thermally released by the TM centers [136]. At higher TM concentrations when the average distance becomes equal to the effective Bohr radius, the overlap of the effective-mass-like states enables to mediate ferromagnetic interaction [11, 39]. At even higher TM concentrations, the impurity band eventually merges with the VB and the material becomes metallic. Here, the coupling between TM spins is mediated by p–d kinetic exchange [137].

The just outlined coupling mechanisms have been studied mainly for (Ga,Mn)As [11, 137–139] where the ground state of the neutral Mn acceptor represents an effective-mass-like state with the hole moderately bound to Mn^{2+} (E_B = 112.4 meV) [140]. The binding energies of the hydrogenic [Fe^{2+}, h] state in III–V materials are only in the range of 40 meV (see below) enabling long-range interactions at lower concentrations. On the other hand, the transient shallow Fe acceptor state [Fe^{2+}, h] in fact is an excited state that may relax into Fe^{3+}. The exact type and magnitude of the interaction between the Fe^{2+} center and the bound hole is analyzed in Section 4.3.3.

4.2 Observing and describing the [Fe^{2+}, h] state The effective-mass-like state [Fe^{2+}, h] can be detected by optical experiments. It is observed in the form of weak sharp features near the photoionization threshold of ab-

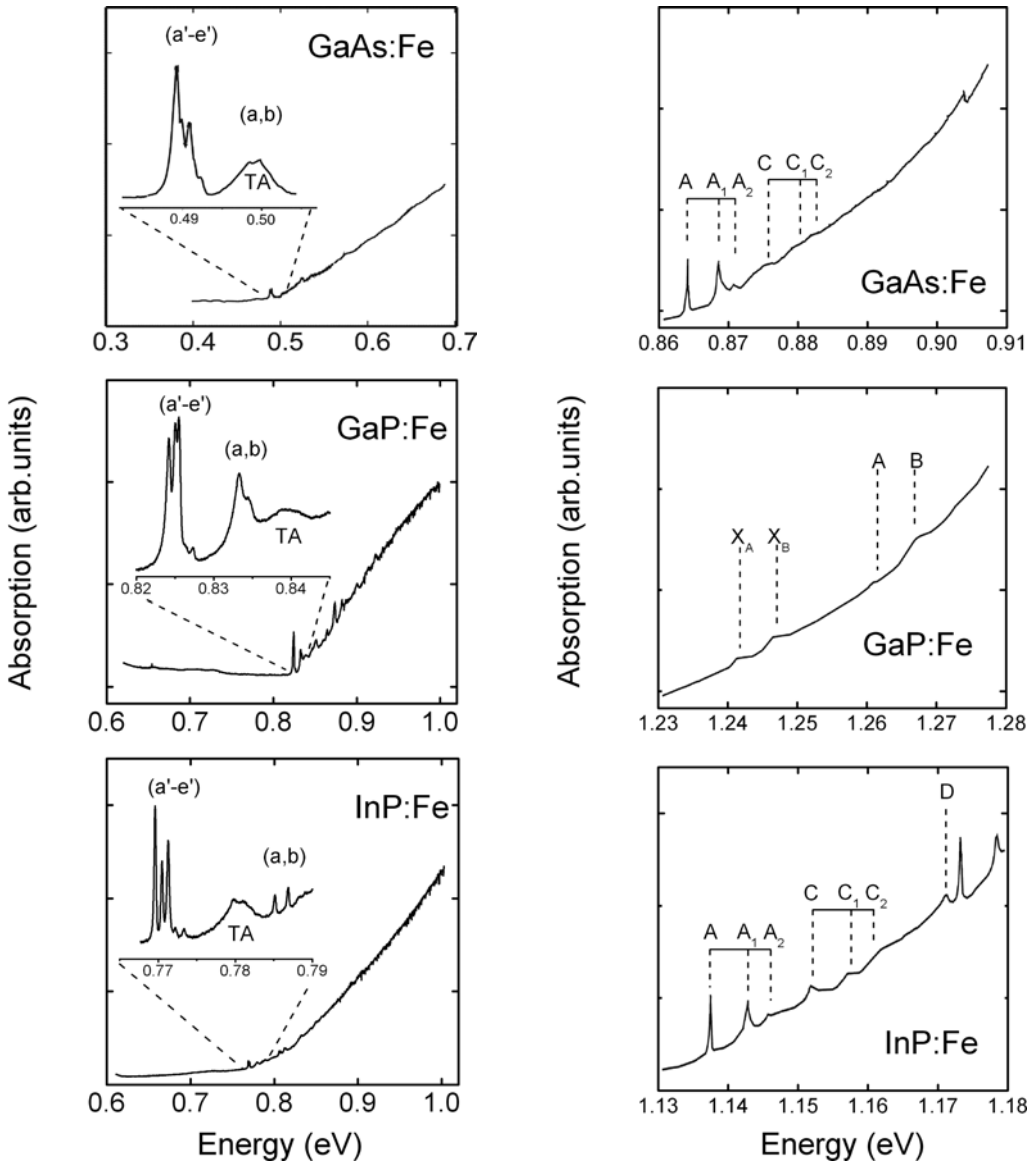

a) $Fe^{3+} + h\nu \rightarrow [Fe^{2+}(^5E), h]$ b) $Fe^{3+} + h\nu \rightarrow [Fe^{2+}(^5T_2), h]$

Figure 14 Absorption spectra of Fe doped GaP, InP and GaAs at $T = 45$ mK. The fine features at the $Fe^{3+/2+}$ photoionization thresholds represent the CT process $Fe^{3+} + h\nu \rightarrow [Fe^{2+}, h]$. (a) The low-energy peaks represent CT processes involving the Fe^{2+} ground state ^5E. (b) The high-energy peaks represent CT processes involving the excited state $^5T_2$.

sorption (Fig. 14) and PLE (Fig. 9) spectra. A resonant photon ionizes the neutral defect and the free carrier stays with the ion. For Fe in III–V compounds:

$$Fe^{3+}(^6A_1) + h\nu \rightarrow [Fe^{2+}, h]. \quad (8)$$

The difference between the ionization energy and $h\nu$ in Eq. (8) equals the binding energy E_b of the hydrogenic state. A potential theoretical description of the resulting bound state is given by a work by Baldereschi et al. who modeled shallow acceptors using effective-mass theory (EMT) and central cell correction [127]. A comparison with experimental data obtained for various systems of bound holes yields a general phenomenon: While there is good agreement of experiment and theory concerning excited EMT states, the experimentally found absolute values of the binding energy of the hole in the EMT ground state are systematically smaller than predicted by EMT (Fig. 22). The reason is that the closed shell situation of shallow acceptors considered by Baldereschi et al. differs considerably from the open shell configuration of an ionized TM impurity. This fact was modeled successfully by Fleurov taking into consideration hybridization effects between the d-orbitals and VB wave functions. Such effects cause the Coulomb potential $V(\boldsymbol{r})$ and the blown up d-orbitals of the ionized center to smear over the neighboring lattice sites.

The results are a larger trapping cross section and a smaller binding energy of holes localized at the ion, i.e., the s-like EMT ground state [128]. Such extended wave functions of the combined [Fe^{2+}, h] state are predicted to potentially enable spin-coupling between isolated TM ions [6].

4.3 Detailed analysis of the [Fe^{2+}, h] state In the following we will give a summary of the numerous studies on the well established bound state [Fe^{2+}, h] in InP, GaP and GaAs and we will complement it with new results bringing clarity into the discussion about an unambiguous assignment of the observed peaks.

The bound state was reported first by Juhl et al. for InP:Fe [121]. However, they interpreted their spectra which are similar to Fig. 14 as an exciton bound to Fe^{3+}. The best argument against this interpretation is the observation of a strong coupling on defect specific vibrational modes with energies typical for the Fe^{2+} center [73, 85] (see Section 5 for defect specific vibrational modes). It is generally accepted, that the five lines (a′–e′) in Fig. 14(a) represent the bound state [Fe^{2+}, h] with Fe^{2+} in its ground state, ^5E, and with the hole in its EMT ground state $1S_{3/2}(\Gamma_8)$ where Γ_8 is the symmetry of the valence band [73, 124, 126]. The five-fold structure is correlated to the spin–orbit splitting of the $Fe^{2+}(^5E)$ state (Section 3.3.4). Here, the splitting is reduced by a factor of about 0.5 which corresponds to a reduction of the spin–orbit coupling parameter λ by about 0.7. This effect is approximately twenty percent stronger in GaP. Pressel et al. explain the reduction of the spin–orbit coupling by the hole in an s-like ground state having a non vanishing probability of finding at the Fe^{2+} center ($\Psi(0) \neq 0$). Therefore, it might influence the d-electrons via spin–spin interaction or Jahn–Teller effect [73, 124, 126]. On the basis of temperature and pressure dependent measurements, we will show in Section 4.3.3 that this simplified model of the bound state [Fe^{2+}, h] as a superposition of the wave functions of Fe^{2+} and a Γ_8-VB-hole is insufficient as it neglects interactions between the VB hole and the core holes.

There is still some debate about the correct interpretation of further lines occurring in Fig. 14 in the context of bound states [Fe^{2+}, h] with the hole in excited EMT states and/or with Fe^{2+} in its excited state $^5T_2$ [73, 123, 124, 126]. In order to address these issues we carried out stress and temperature (mK) dependent absorption measurements on Fe doped GaP, InP and GaAs samples.

4.3.1 Experimental details Stress dependent optical absorption experiments were performed using a BOMEM DA3.01 Fourier-transform spectrometer equipped with a CaF_2 beam splitter and a cooled InSb detector. The samples were mounted in a stage allowing the application of compressive uniaxial stress. A temperature of 6 K was achieved by a continuous flow He cryostat.

Temperature dependent optical absorption experiments were carried out at mK temperatures using calorimetric absorption spectroscopy (CAS). The CAS spectrum is the increase of sample temperature versus the excitation photon energy. It is sensitive to non-radiative relaxation processes by detecting the increase of sample temperature caused by the generation of phonons after optical excitation. The CAS setup is located inside a $^3He/^4He$ dilution refrigerator cryostat (Oxford Instruments). A halogen lamp in combination with an 1 m grating monochromator (Jarrel Ash) was employed as tunable excitation source. Details of the experimental setup are described in Ref. [141].

The InP:Fe, GaP:Fe and GaAs:Fe samples were taken from bulk crystals grown by the liquid encapsulation Czochralski (LEC) method. Iron was added to the melt. With an Fe concentration of about 1×10^{17} cm^{-3} the samples are semi-insulating with the Fermi-level pinned to the $Fe^{3+/2+}$ acceptor level, i.e. both charge states 3+ and 2+ are present at equilibrium. For stress experiments oriented samples with the dimensions $2 \times 4 \times 10$ mm^3 were prepared with the long axis parallel to the [100], [110] and [111] direction. Samples for CAS had the dimensions $1 \times 4 \times 10$ mm^3.

4.3.2 Experimental results

4.3.2.1 Temperature dependent measurements The fine structure lines displayed in the insets of Fig. 14(a) were studied in detail by CAS at varying temperatures. In the temperature range between 0.5 K and 15 K, the intensities of the lines (a′–e′) and (a, b) stayed constant. The absence of thermalization effects confirms that the these lines represent excited states of the observed transition.

The temperature dependence of these lines in the mK range is shown in Fig. 15 for GaP and InP. Below 200 mK each line exhibits an individual temperature behavior. In all three materials the thermalization of each single line

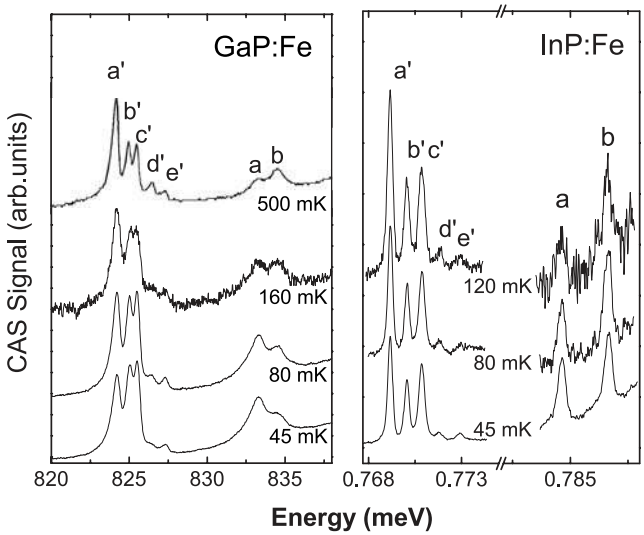

Figure 15 Temperature dependent CAS spectra of the fine structure lines (a′–e′) and (a, b) representing transitions $Fe^{3+} \rightarrow [Fe^{2+}(^5E), h]$ at mK-temperatures. The single lines exhibit individual temperature behaviors.

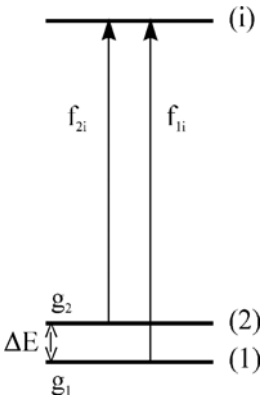

Figure 16 Sketch of an absorption transition with a two-fold split ground state and one excited state.

exhibits a similar behavior which is the most pronounced for GaP.

The temperature dependent behavior in the mK range must be the result of thermalization effects in the ground state. At mK temperatures the thermal activation energy is only a few μeV. Hence, the splitting of the ground state is much smaller than the linewidth (~1 meV). Consequently, each line represents a superposition of transitions with a common final state but individual ground states separated by a few μeV. In order to gain insights we assume a simple model outlined in Fig. 16. The ground state is split by ΔE into two levels with degeneracies g_1 and g_2, respectively. The population ratio N_2/N_1 of the two sub-levels is given by Boltzmann-statistic.

$$\frac{N_2}{N_1} = \frac{g_1}{g_2} e^{-\frac{\Delta E}{kT}}. \tag{9}$$

If the respective oscillator strengths of the transitions are f_{1i} and f_{2i}, then the intensity of one absorption line as a function of temperature is given by

$$I_i = \frac{A f_{1i}}{1+\frac{g_2}{g_1} e^{-\frac{\Delta E}{kT}}} \left(1+\frac{f_{2i}}{f_{1i}} \frac{g_2}{g_1} e^{-\frac{\Delta E}{kT}}\right), \tag{10}$$

Table 8 Parameters of Eq. (10) determined by fitting the temperature dependencies of lines (a′–e′) and (a, b) in Fig. 17.

	a′	b′	c′	d′	e′	a	b
GaP : Fe							
ΔE (μeV)	14.5	14.5	14.5	14.5	14.5	14.5	14.5
g_2/g_1	2	2	2	2	2	2	2
f_{2i}/f_{1i}	1.6	0.8	0.5	>40	3	0.2	2.7
$A f_{1i}$	3.5	3.2	4.2	<0.03	0.3	2.2	0.6
InP : Fe							
ΔE (μeV)	8.5	8.5	8.5	8.5	8.5	8.5	8.5
g_2/g_1	2	2	2	2	2	2	2
f_{2i}/f_{1i}	1.52	0.8	0.5	9.2	2.3	<0.02	2
$A f_{1i}$	1.7	1.04	1.55	0.04	0.1	0.23	0.17

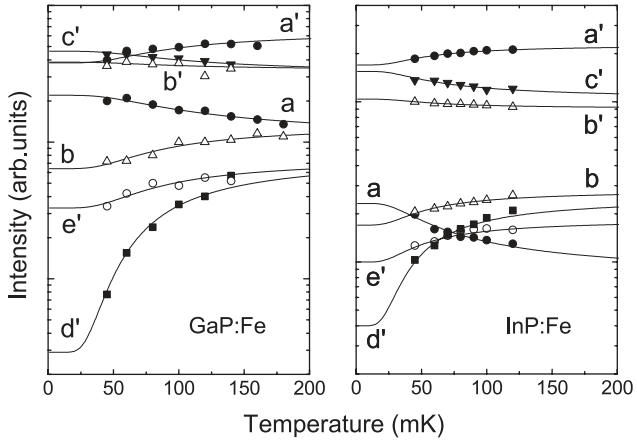

Figure 17 Temperature dependance of the seven fine structure lines (a′–e′) and (a, b) observed in semi-insulating GaP and InP (Fig. 15). The solid curves represent fits using Eq. (10) and the parameters compiled in Table 8.

where A is a constant describing the intensity at $T = 0$ K. From Eq. (10) it can easily be seen that the temperature behavior depends on the ratio f_{2i}/f_{1i}. This and other parameters, particularly ΔE, can be determined by fitting the results from temperature dependent experiments according to Eq. (10). The results for GaP and InP are displayed in Fig. 17 and the used parameters are summarized in Table 8. A simultaneous fit of all seven lines is possible only for a degeneracy ratio of $g_2/g_1 = 2$. The determined ground state splittings of 15 ± 3 μeV and 8 ± 2 μeV for GaP and InP, respectively, are in good agreement with ESR data for the splitting of the Fe^{3+}($^6A_1$) ground state (see Table 2, Section 3.2.1). No absolute values of the oscillator strengths can be given since the exact Fe^{3+} concentration of our samples is unknown.

4.3.2.2 Uniaxial stress experiments Uniaxial stress experiments were performed to obtain information on the electronic character of the bound states behind lines displayed in Fig. 14. Under uniaxial pressure along the [100]-, [110]- or [111]-axis, the crystal symmetry for Fe on cation site is reduced from T_d to D_{2d}, C_{2v} or C_{3v}, respectively. If the bound state can be described by a superposition of a hole and an Fe^{2+} center, then the total stress induced splitting should equal the splitting of the Fe^{2+} states times the splitting of the Γ_8-VB-hole state. The splitting of the Fe^{2+} states ^5E and $^5T_2$ under uniaxial pressure is presented in Section 3.3.7. The fourfold degenerate Γ_8 state of the valence band hole splits into two twofold degenerate levels under stress in any direction. Consequently, twofold and fourfold splittings are expected.

Figure 18 shows exemplary stress dependent absorption spectra of the lines (a′–e′) for different uniaxial stress conditions. Small absorption coefficients and reduced intensities through splitting made the stress dependent measurements difficult to perform and it cannot be ruled out that very weak lines were not detected. While detailed

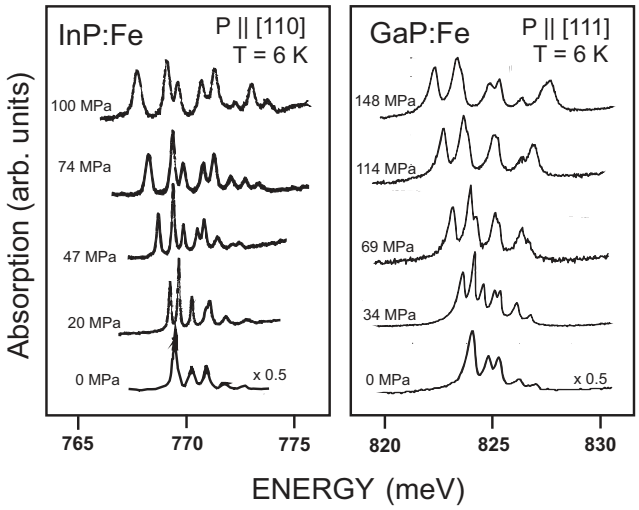

Figure 18 Exemplary absorption spectra of the quintet (a′–e′) in GaP and InP under different uniaxial pressure conditions.

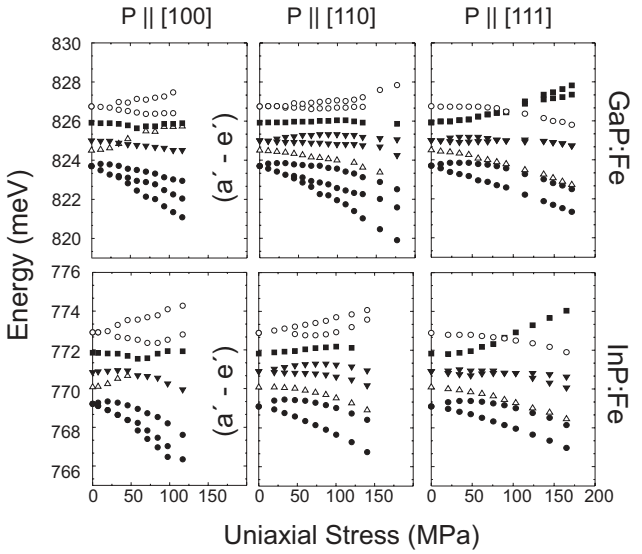

Figure 19 Pressure-behavior of the quintet (a′–e′).

spectra could be recorded for the lines (a′–e′) in InP and GaP, the split lines (a, b) could be resolved only for InP. No distinct polarization of the split lines was observed confirming that each line is a superposition of two lines originating from the fine structure splitting of the $Fe^{3+}(^6A_1)$ ground state.

The complete observed stress behavior of the lines (a′–e′) in InP and GaP is illustrated in Fig. 19 and is very similar for the two materials. Threefold splittings (e.g. line a′, $P \parallel [100]$) and line shifts (e.g. line b, $P \parallel [100]$) are in considerable disagreement with the simple model of a superposition outlined above.

The stress-induced splitting of the lines a, b, A and A_1 in InP is shown in Fig. 20. In the following, the observed splitting is compared to the expected one outlined above. $P \parallel [111]$: The lines a and b exhibit a twofold splitting of equal amplitude (9.5 meV/GPa) which can be attributed to the splitting of the hole, as the splitting of the $\Gamma_4(^5E)$ state is too small to be resolved (see Section 3.3.7). $P \parallel [110]$: Both lines a and b exhibit the expected behavior, a splitting of 10.0 meV/GPa on account of the hole (lines a, b) and a splitting of 6 meV/GPa of the $Fe^{2+}(\Gamma_4(^5E))$ state (line b). The latter value is in good agreement with the splitting of 7 meV/GPa obtained from intra-center luminescence [87]. $P \parallel [100]$: Although a splitting similar to $P \parallel [110]$ is expected, here, only a twofold splitting is detected for line b and none for line a. Further splitting may have been outshone by the noisy background. For the interpretation of

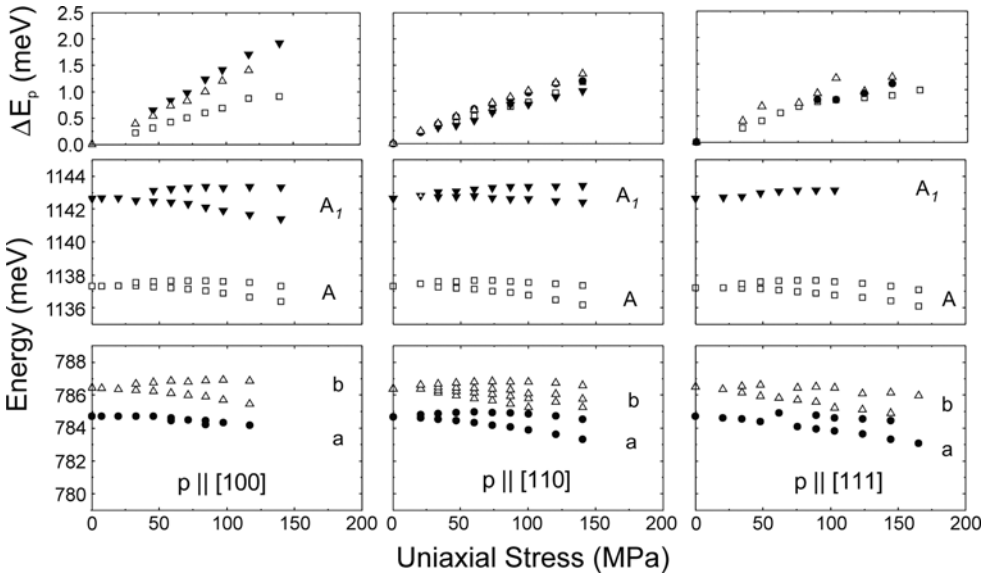

Figure 20 Stress behavior of lines a, b, A, A_1 in InP. In the top row, the magnitude of the stress induced splitting ΔE_p is displayed.

the lines A and A_1 the splitting of the $Fe^{2+}(\Gamma_5(^5T_2))$ state under stress has to be taken into account. For any direction a twofold splitting was established (Section 3.3.7). Therefore, a fourfold splitting is expected. However, only the twofold hole splitting is observed (Fig. 20).

Concerning a quantitative analysis of the stress behavior of lines a, b, A and A_1, the splitting of the valance band hole state under stress P is described by deformation potentials β and δ [143]. The splitting ΔE_h of the free hole state Γ_8 is given by:

$$P \| [100]: \quad \Delta E_h = 2\beta(S_{11}/S_{12})\, P\,, \tag{11}$$

$$P \| [110]: \quad \Delta E_h = [\beta^2(S_{11}/S_{12})^2 + \delta^2 S_{44}^2]^{\frac{1}{2}}\, P\,, \tag{12}$$

$$P \| [111]: \quad \Delta E_h = \left(\frac{1}{\sqrt{3}}\delta S_{44}\right) P\,, \tag{13}$$

where S_{ij} are elastic modules. For InP their values are: $S_{11} = 1.65 \times 10^{-2}$ GPa^{-1}, $S_{12} = -0.59 \times 10^{-2}$ GPa^{-1} and $S_4 = 2.17 \times 10^{-2}$ GPa^{-1} [144]. The deformation potentials β and δ can be determined from the experimental data. The observed energetic splitting ΔE_p is depicted in the top row of Fig. 20. For the lines a and b it can be successfully fitted for all three directions with the values $\beta' = 0.245$ eV and $\delta' = 0.76$ eV. Lines A and A_1 show slight deviations from those fits indicating that the coupling between the hole and Fe^{2+} is different for the ground and excited state of Fe^{2+}. Compared to the deformation potentials of the free exciton in InP (β = 1.55 eV, δ = 4.2 eV) [145], the values of the bound hole are reduced by the factor $\beta'/\beta \approx \delta'/\delta \approx 0.17$. Such a reduction of the deformation potentials is common for bound states [146].

The results of the stress dependent experiments can be summarized as follows: While the stress behavior of the lines a, b, A and A_1 is in reasonable agreement with a superposition of hole and Fe^{2+}, the one of the lines (a′–e′) is not. Hence, a more sophisticated model is required to describe the bound state.

4.3.3. Discussion

4.3.3.1 The ground state The temperature dependence of the intensity of the absorption lines (a′–e′) and (a, b) in the mK range can be explained assuming a ground state consisting of two sub-levels. The found distance between them amounts to 15 ± 3 μeV and 8 ± 2 μeV for GaP and InP, respectively, which is in good agreement with the splitting of the $Fe^{3+}(^6A_1)$ state determined by ESR (see Table 2, Section 3.2.1). The Fe^{3+} ($^6A_1$) state is split by second-order spin–orbit and spin–spin interaction into two levels of Γ_7 and Γ_8 symmetry separated by $\Delta E = 3a$ (a is the fine structure parameter). The correct order cannot be obtained from ESR though. The Γ_7 state is twofold and the Γ_8 state fourfold degenerate. Hence, the found ratio of degeneracies $g_2/g_1 = 2$ leads to the conclusion that the Γ_8 level is located above the Γ_7 level.

4.3.3.2 The bound state [$Fe^{2+}(^5E)$, h] In this section the bound state [$Fe^{2+}(^5E)$, h] will be discussed which is the final state of the transitions represented by lines (a′–e′) and (a, b). First we will focus on the lines a and b.

In agreement with previous works [121, 124], the lines a and b in InP are assigned to the formation of a bound state [$Fe^{2+}(^5E)$, h] with the hole in its first excited EMT state, $2P_{3/2}(\Gamma_8)$ and the Fe^{2+} center in the states $\Gamma_1(^5E)$ and $\Gamma_4(^5E)$, respectively. Key arguments are the small linewidth and the energy spacing equal to the spin–orbit splitting of the $Fe^{2+}(^5E)$ state (Section 3.3.4). The stress behavior of the lines (a, b) is compliant with a superposition of Fe^{2+} and a Γ_8-VB-hole supporting the interpretation as a weakly bound and thus excited hole.

For the following reasons we interpret the lines (a, b) in GaP the same way as in InP despite missing stress experiments for GaP and contrary assignment in previous works as TA phonons of the lines (a′–e′) [73]: (i) The lines are too narrow to be TA phonon replica. (ii) No analogous phonon structure is found in InP although other phonon satellites of lines (a′–e′) are quite similar in both materials. (iii) The lines (a, b) show the same temperature dependence in both materials. (iv) The temperature behavior of lines (a, b) is contrary to that of lines (a′, b′). The association of lines (a, b) in GaP with TA phonons is based on a complex model including a Jahn–Teller effect [73]. However, a significant impact of a Jahn–Teller effect is rather unlikely given the weak phonon coupling of the complex. Moreover, the assignment of the weak resonances around 846 meV to be the analogue to the lines (a, b) in GaP does not comply with an over-all model of EMT states. This will be discussed below.

Concerning lines (a′–e′), the model of a superposition of a Γ_8 hole in the VB and the $Fe^{2+}(^5E)$ center is not capable to explain the stress behavior of these lines. Also the inverse temperature dependence of lines (a′, b′) in comparison with lines (a, b) necessitates a revised and more comprehensive model of the bound complex that also holds for the interpretation of lines a, b, A and A_1.

The quintet (a′–e′) can be explained conclusively by the model of a modified spin–orbit interaction (Section 4.3). However, the fundamentals of the formation of the [Fe^{2+}, h] complex are not taken into account in this model. The interaction between the Fe^{2+} core and the hole is affected by spin–spin coupling and exchange interaction. The magnitude of these interactions scales with the overlap of the Fe^{2+} and hole wave functions. An evaluation of the magnitude of the exchange interaction is crucial as it represents one of the major mechanisms of spin-coupling between free carriers and TM centers (see above).

The electronic structure of the [$Fe^{2+}(^5E)$, h] bound states under the influence of exchange interaction is modeled in Fig. 21 for three different cases. If the exchange interaction is negligible compared to the spin–orbit interaction, then the fine structure of the bound state will be similar to that of the unperturbed $Fe^{2+}(^5E)$ state. In case of a weak exchange interaction that cannot be neglected, the re-

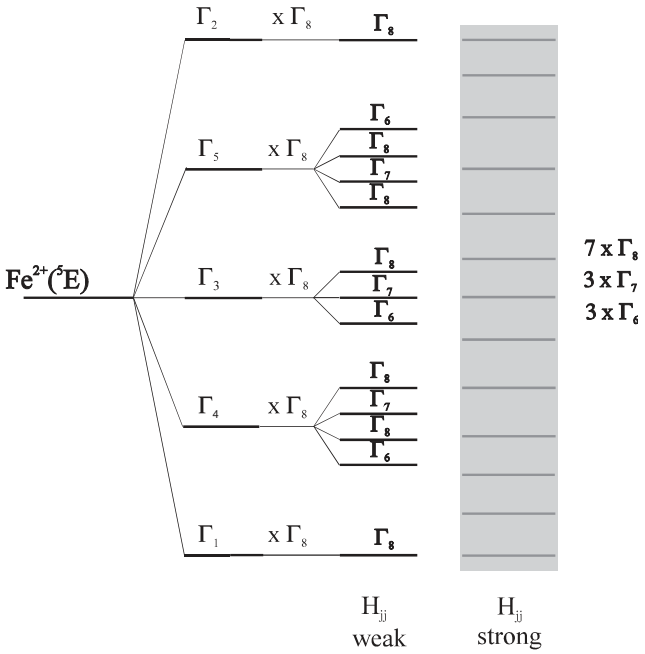

Figure 21 Symmetries and relative energies of $[Fe^{2+}(^5E), h]$ states under consideration of weak and strong exchange interaction between the $Fe^{2+}(^5E)$ spin–orbit states and the Γ_8-VB-hole. For a strong influence of the exchange interaction, only rough predictions about the symmetries of the resulting states can be made.

sulting splitting and symmetries can be acquired from the Kronecker-product of the Γ_8-VB-hole and the $Fe^{2+}(^5E)$ states. In case of a strong exchange interaction that is of the same order of magnitude as the spin–orbit coupling, the resulting states cannot be calculated from hole and Fe^{2+} states without major effort. In the latter case, a maximum of thirteen states of Γ_6, Γ_7 and Γ_8 symmetry are expected from group theory considerations.

The observation of five equidistant lines suggests that the $[Fe^{2+}(^5E), h]$ states are dominated by the fine structure of the $Fe^{2+}(^5E)$ state ruling out effects of a strong exchange interaction. This leads us to the following comprehensive model explaining all experimental findings: (i) The presence of the VB hole at the Fe^{2+} core leads to a reduced spin–orbit interaction (outlined above) and thus to a reduced splitting of the $Fe^{2+}(^5E)$ state. (ii) The impact of the exchange interaction between the VB hole and the Fe^{2+} core cannot be neglected and governs the symmetry of the resulting states.

That leaves the determination of the symmetries of the five EMT ground states and a detailed comparison with the experimental results. The discussed transitions have initial states $(Fe^{3+}(^6A_1))$ of Γ_7 and Γ_8 symmetry (Section 4.3.3). Of possible transitions between Γ_7 and Γ_8 initial and Γ_6, Γ_7 and Γ_8 final states only the $\Gamma_7 \leftrightarrow \Gamma_7$ transition is forbidden. As a result of the Kronecker-product, lines a′ and e′ can easily be assigned to states of Γ_8 symmetry. The intensity of line d′ has a vanishing intensity at lowest temperatures where only the $Fe^{3+}(\Gamma_7(^6A_1))$ state is populated and rises quickly with increasing temperature where also the $Fe^{3+}(\Gamma_8(^6A_1))$ state is populated thermally (Table 8, Fig. 17). Consequently, the final state must be of Γ_7 symmetry. Lines b′ and c′ must represent transitions into states of Γ_6 or Γ_8 symmetry since they are very pronounced even at lowest temperatures (Table 8, Fig. 17). The stress behavior of the lines provide further clarity. From the appropriate multiplication table in Ref. [147] we see that for a reduction of symmetry from T_d to C_{2v}, C_{3v} or D_{2d}, a Γ_8 state splits into two or three levels whereas Γ_6 and Γ_7 states do not split but only change symmetry. A comparison with Fig. 19 delivers the symmetries of the lines (a′, b′, c′, d′, e′) to be (Γ_8, Γ_6, Γ_8, Γ_7, Γ_8), respectively. The only experimental result that remains unclear is the threefold splitting of line a′ under certain pressure conditions (Fig. 19).

In order to determine the binding energy (E_b) of the bound state $[Fe^{2+}, h]$ a comparison with the EMT model is depicted in Fig. 22. The observed absorption lines are assigned to EMT states by dashed lines. The EMT binding energies were taken from Ref. [127]. Line a was used as a reference because its final state was shown to be in good agreement with the first excited EMT state $2P_{3/2}$. Both the spectra and the EMT axes were shifted so that the ionization thresholds ($E_b = 0$) of all materials line up with each other.

The experimentally found position of the ground state is shifted to higher energies (weaker bonding) as was predicted by Fleurov [128]. While a shift of 3.9 meV and 3.2 meV for InP and GaAs, respectively, is relatively small, it is rather large for GaP (17.7 meV). The larger shift for GaP suggests a stronger localization of the ground state hole at the core. This assumption is supported by the larger reduction of the spin–orbit coupling in GaP discussed in the first part of Section 4.3. The stronger localization of the $1S_{3/2}(\Gamma_8)$ hole at the Fe^{2+} core in GaP is also reflected by the larger binding energy (stronger) predicted by EMT [127].

The weak resonances in the GaP spectrum labeled (a_1, b_1) represent the second excited EMT state, $2S_{3/2}(\Gamma_8)$, of the hole. Due to the s-type wavefunction this state is shifted to smaller binding energies (weaker) as well. This shift (6.7 meV) is not as large as that of the 1S state because of the smaller probability of finding at the core. The binding energies of the $[Fe^{2+}, h]$ complex with the hole in the EMT ground state determined from the just outlined assignment are 31.3 meV for InP, 28.1 meV for GaP and 22.5 meV for GaAs.

Unfortunately, the same effective-mass-like state in GaN could not be resolved as well as in GaP, InP and GaAs [12]. Furthermore, no EMT calculations as detailed as in Ref. [127] exist for acceptor impurities in GaN. For those two reasons, we can only attempt a tentative determination of the binding energy in GaN. We calculate the binding energy using simplified EMT: $E_b = -Rm^*/(\varepsilon^2 n^2)$, with the Rydberg constant $R = 13.6$ eV, the relative effective mass of the hole in GaN $m^* = 83$ [148], effective di-

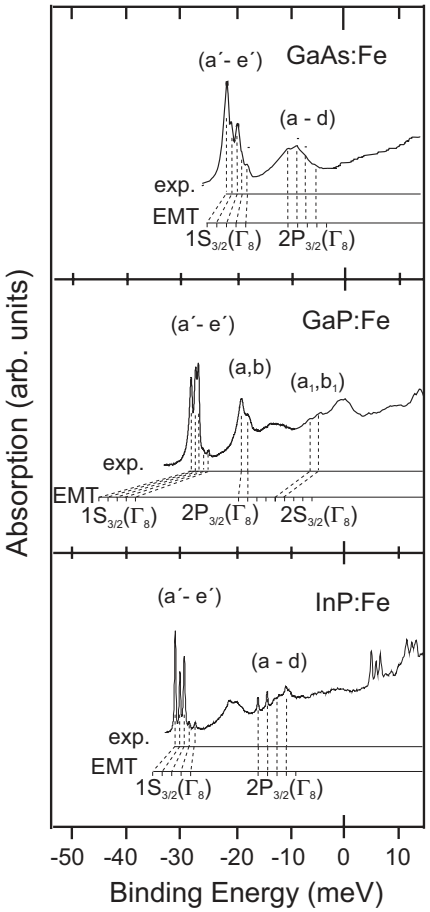

Figure 22 Comparison and association of the fine structure lines of the (Fe^{2+}(^{5}E), h) complex with EMT states. The EMT values are taken from Ref. [127]. Line a was taken as a reference. The lines (a–d) are in good agreement with the $2P_{3/2}(\Gamma_8)$ EMT state. The binding energies of the s-type EMT states $1S_{3/2}(\Gamma_8)$ and $2S_{3/2}(\Gamma_8)$ are shifted to higher energies (weaker bonding) because of hybridization effects of the Fe^{2+} d-orbitals with the ligands. The reduced spin–orbit splitting is caused by the presence of the hole at the Fe^{2+} core partially quenching the spin–orbit coupling.

electric constant $\varepsilon = 9.5$ and the "main" quantum number n. We interpret the resonances 24 meV and 37 meV above the ground state at 2.812 eV [12] as the first ($n = 2$) and second excited ($n = 3$) EMT states, respectively. For $n = 1, 2, 3$, we receive $E_b = 125, 31, 14$ meV, respectively. The difference between the last two values (17 meV) is larger than found experimentally (13 meV) which can be explained by the first excited shifting stronger to smaller binding energies. If we assume the second excited state to remain unshifted, we obtain a binding energy of the ground state of 51 meV. This result is in good agreement with the value of about 50 meV derived from the distance to the photoionization threshold [12]. Because of the coarse model applied above this new value cannot be considered more accurate. A binding energy of ≈50 meV means a shift of 75 meV according to our model. This is one order of magnitude larger than for GaP, InP and GaAs. This could be explained by the relatively small lattice constant leading to a stronger hybridization of the Fe^{2+} d-orbitals with the VB [128].

4.3.3.3 The bound state [Fe^{2+}($^5T_2$), h] In this section the bound state [Fe^{2+}($^5T_2$), h] will be discussed which is the final state of the transitions represented by lines (A, A_1, A_2), (C, C_1, C_2) and D in Fig. 14(b).

The lines A, C and D in InP and GaAs are assigned to the formation of [Fe^{2+}($^5T_2$), h] complexes with the hole in its first excited EMT state $2P_{3/2}(\Gamma_8)$ and the Fe^{2+} center in the first three $^5T_2$ states with reasonable transition probabilities, respectively. These $^5T_2$ states are the result of the strong Jahn–Teller coupling on the $^5T_2$ spin–orbit levels discussed in Section 3.3.5. The mentioned transition probability is the one for transitions starting at the Fe^{3+}($^6A_1$) state. These are unknown since relative intensities have only been calculated for transitions starting at the Fe^{2+}($^5E(\Gamma_1)$) state [78]. Thus, the only thing we can tell for certain is that the Fe^{2+}($^5T_2$) state involved in the bound state behind the lines (A, A_1, A_2) is the Γ_5 state which remains unaffected by the Jahn–Teller effect (Section 3.3.5). The Fe^{2+}($^5T_2$) states involved in the lines (C, C_1, C_2) and D are unclear. The above assignment is supported by the

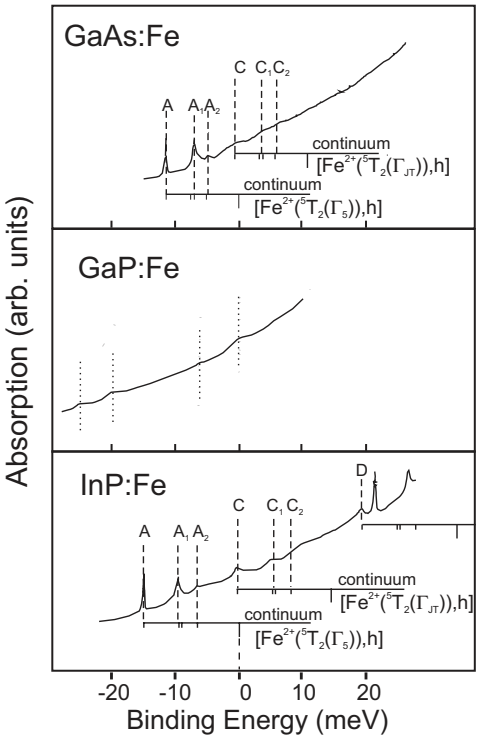

Figure 23 Assignment of the fine structure lines of the (Fe^{2+}($^5T_2$), h) complex to EMT states of the hole. On the inserted EMT axes, the positions of the first four excited states $2P_{3/2}(\Gamma_8)$, $2S_{3/2}(\Gamma_8)$, $2P_{5/2}(\Gamma_8)$ and $2P_{5/2}(\Gamma_7)$ are indicated as well as the ionization thresholds. The EMT ground state $2S_{3/2}(\Gamma_8)$ does not appear in these spectra for reasons given in the text. The EMT values are taken from Ref. [127].

same facts as the lines (a, b) and by agreement with previous studies [124]. A comparison with the EMT model (Fig. 23) evidences that line A_1 represents the second and third excited EMT states $2S_{3/2}(\Gamma_8)$ and $2P_{5/2}(\Gamma_8)$ and line A_2 represents the higher excited EMT state $2P_{5/2}(\Gamma_7)$. The same holds for the lines C_1 and C_2. The observed energy spacings are in excellent agreement with EMT calculations by Baldereschi [127].

In contrast to the $[Fe^{2+}(^5E), h]$ complex, here, no EMT ground state involving the $Fe^{2+}(^5T_2)$ center is observed in either of the EMT series $(A-A_2)$ or $(C-C_2)$. This phenomenon can be explained plausibly: As observed for the $[Fe^{2+}(^5E), h]$ complex (lines $(a'-e')$), the spin–orbit splitting of the $^5T_2$ state is reduced by the presence of the hole in the s-type EMT ground state $1S_{3/2}(\Gamma_8)$. For the $^5T_2$ state this would mean that the modified lowest $^5T_2$ state Γ_5 is shifted to an energy above line A making the EMT ground state thermodynamically unstable. Hence, if transitions into such a state occur the absorption lines are extremely broadened by the short lifetime [124]. The same should hold for the second excited EMT state $2S_{3/2}(\Gamma_8)$. Consequently, its absence at the position of lines A_1 and C_1 is not a matter of poor resolution but founded on the reasons named above.

No $[Fe^{2+}(^5T_2), h]$ complexes were observed for GaP. The weak resonances X_A, X_B, A and B found at the onset of the high-energy CT band (Fig. 14(b)) were interpreted by Pressel et al. as ground and excited EMT states [73]. However, this interpretation is very arguable as it is in harsh disagreement with our temperature dependent experiments and the findings from InP and GaAs.

Knowing the binding energy E_b of the $[Fe^{2+}, h]$ state the position of the $Fe^{3+/2+}$ CT level within the band gap can be determined from the observed $[Fe^{2+}, h]$ peaks. Because of their shape this method is more accurate than fitting the photoionization threshold. The resulting positions as measured from the VB maximum are 800.6 meV, 851.8 meV and 510 meV for InP, GaP and GaAs, respectively. These values differ from previous works. In Ref. [124] the spectra of InP were accidently compared with the EMT binding energies of GaP. A different CT energy in GaP is stated in Ref. [73] on the basis of a different interpretation of the lines (a, b) and TA phonon replica (Section 4.3.3).

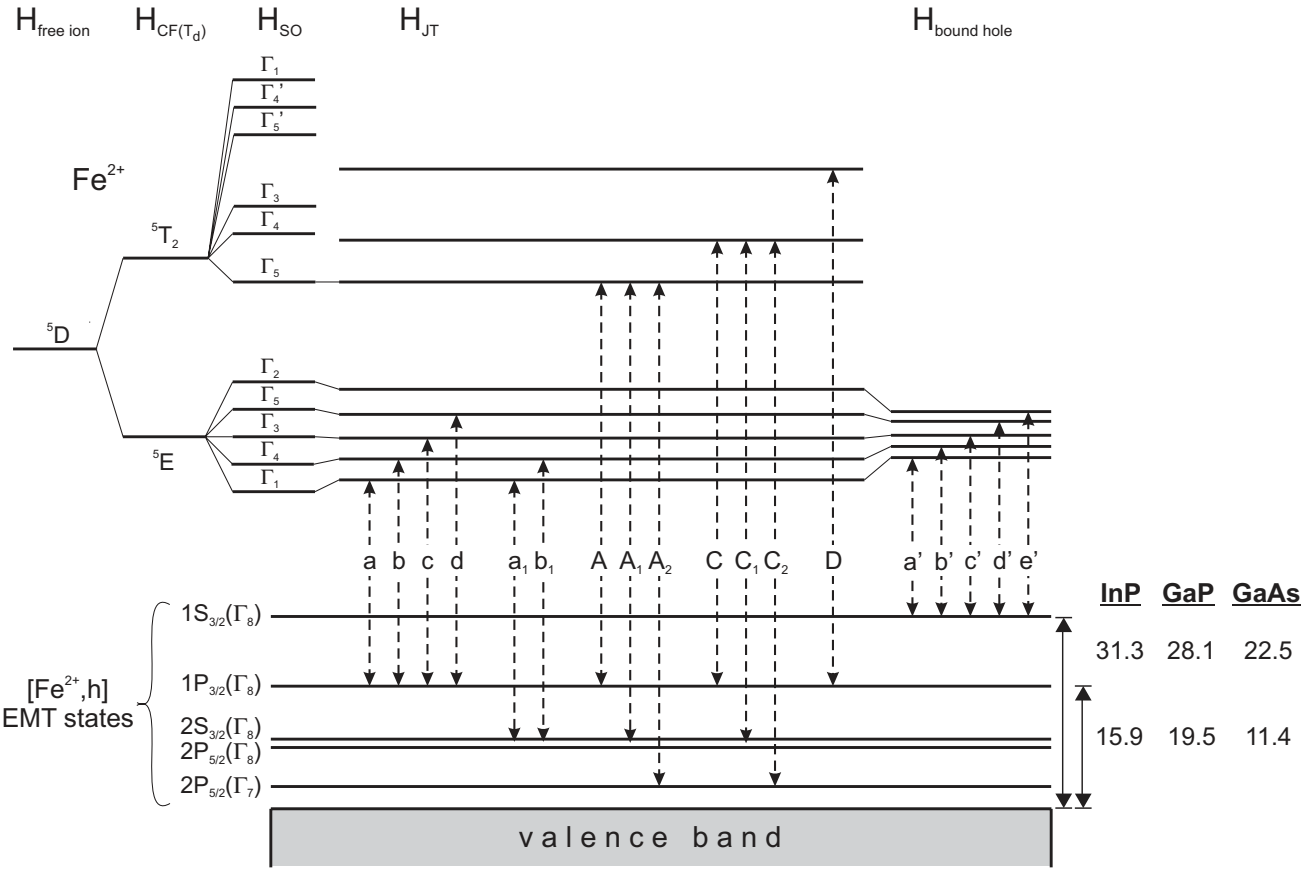

Figure 24 Assignment of the CT lines found in Fig. 14 to bound states that are characterized by the electronic state of the involved Fe^{2+} center (top) and an EMT state (bottom). The Fe^{3+} ground state of the transitions is not depicted. The approximate position of the transient acceptor state established by the bound state is also shown. The binding energies on the right are given in meV. The scheme is not to scale. In fact, the energies of EMT states are larger than those of the $Fe^{2+}(^5E)$ splitting and smaller than those of $^5T_2$. Of the numerous $^5T_2$ Jahn–Teller states only the ones involved in bound states are included.

If we want to estimate the extent of the EMT ground state [Fe^{2+}, h] state we need to keep in mind that it does not comply exactly with EMT. However, assuming an effective-mass-like state the effective radius can be sized up by $a^* = a_B R/(E_b \varepsilon^*)$ from the found binding energy E_b (in eV), with the Bohr radius a_B, the Rydberg constant R and the effective dielectric constant ε^*. Values for the $1S_{3/2}$ state of 2.3 nm, 1.8 nm, 2.5 nm and 1.5 nm for GaP, InP, GaAs and GaN, respectively, indicate that the bound hole should still be characterized by VB properties.

4.3.4 Concluding remarks The bound states found in InP, GaP and GaAs are summarized in Fig. 24. The situation depicted in Fig. 24 should be similar in other materials, particularly in GaN.

Regarding carrier mediated spin-coupling, our findings yield the following implications. The various bound states [Fe^{2+}, h] depicted in Fig. 24 provide scores of shallow acceptor levels. The at least weak exchange interaction within the s-type EMT states, $1S_{3/2}(\Gamma_8)$ and $2S_{3/2}(\Gamma_8)$, should facilitate spin-coupling between the hole and the Fe^{2+} center. From the determined extent of the bound state, $a^* \approx 2$ nm, the critical Fe concentration N_c, for which an overlap of the wave functions enables a long-range interaction, can be calculated from the Mott criterion $N_c \approx (0.25/a^*)^3 \approx 2 \times 10^{18}$ cm^{-3}. At room temperature, the first excited EMT state should be occupied with an at least four times larger radius potentially enabling extended interactions already at smaller concentrations. At even lower Fe densities, carrier mediated spin-coupling could be established via holes being captured and thermally released by the Fe centers [136]. This coupling mechanism is supported by the relatively small binding energy of the magnitude equal to the thermal energy at room temperature. However, it needs to be kept in mind that the relaxation of the bound state into Fe^{3+} represents a competing process. Unfortunately, the lifetime of this process is still unknown.

5 Fe-specific vibrational modes The different mass of an impurity atom in comparison to the cation it is replacing leads to a change of local vibrational modes. Resulting defect specific vibrational modes have been reported for Fe in GaP, GaAs, InP, GaN, ZnO [12, 46, 72, 84, 85, 149–152]. In General, different charge states and even different electronic states of the same charge state exhibit individual defect specific modes because each electronic configuration results in a different coupling constant in the model of the harmonic oscillator [84, 85].

Such defect specific vibrational modes can be observed by means of Raman spectroscopy or in the form of replica of defect related luminescence or absorption lines. For both methods caution needs to be taken when interpreting new lines arising upon impurity introduction. The presence of a point defect may cause silent lattice modes to become allowed by breaking the translational symmetry of the bulk crystal [153]. Further care needs to be taken when assigning replica of internal transitions. As demonstrated in Section 3.3, alleged replica on account of defect specific vibrational modes may in fact arise from transitions involving vibrational states affected by Jahn–Teller coupling [78]. In order to avoid misinterpretation experimental findings should be compared with theoretical calculations.

Concerning GaP, InP and GaAs, Pressel and coworkers distinguish three different kinds defect specific vibrational modes [46, 72, 84, 85]: Resonant modes (RM) are degenerate with lattice phonon states. Gap modes (GM) are located within the phonon band gap and are characteristic for phosphorous ligands. Local modes (LM) have larger energies than optical lattice phonons. For exact energies of Fe specific vibrational modes in GaP, GaAs, InP, GaN see Refs. [12, 72, 84, 85]. A comparison of these works with theoretical calculations [78, 151] confirms the identity of the found modes.

6 Summary For the realization of spin-coupling in a DMS a detailed quantitative understanding of the electronic states introduced through TM doping is essential. The electronic properties of Fe doped III–V and II–VI compound semiconductors were reviewed and the involved experimental methods were presented.

The $Fe^{3+/2+}$ level is found within the band gap of many materials while the $Fe^{2+/1+}$ level has only been observed in a few and the $Fe^{3+/4+}$ level in none. While the position of the CT levels has mainly been derived from the photoionization threshold, it can be determined with higher accuracy via the effective-mass-like state [Fe^{2+}, h]. To date no CT level has been detected in ZnO. On the basis of trends of the position of the CT levels within related material systems (internal reference rule), predictions about as yet undetected CT levels could be made. The results were discussed against the background of a potential realization of a ferromagnetic coupling in DMS's. The suitability of Fe doped GaN for hole-mediated spin-couping critically depends on whether the $Fe^{3+/4+}$ donor level is found above or below the VB edge. The deep $Fe^{2+/3+}$ donor level in II–VI compounds renders these materials unsuitable for hole mediated spin-coupling.

Detailed term schemes of the Fe ions in tetrahedral and trigonal crystal field symmetry are presented, including hyperfine structure, isotope effects and Jahn–Teller effect. Most of the insights about the respective electronic structure was obtained from the radiative transitions $Fe^{3+}(^4T_1 \rightarrow {}^6A_1)$ and $Fe^{2+}(^5E \rightarrow {}^5T_2)$. The trigonal symmetry in hexagonal crystals can be approximated by a perturbation in the form of an axial distortion of the tetrahedral case. While a weak or intermediate Jahn–Teller coupling was shown to effect most Fe electronic states, the fine structure of the $Fe^{2+}(^5T_2)$ state is significantly altered by a strong Jahn–Teller effect. From the established term-schemes in combination with the positions of the CT levels, we concluded that, except for the effective-mass-like state, no levels close to one of the bands are formed by the Fe impurity.

The collected data indicate small but non-negligible degrees of covalency between Fe and the ligands. It scales with the degree of covalency of the host crystal.

New insights on the shallow effective-mass-like acceptor state [Fe^{2+}, h] could be obtained by means of temperature dependent CAS experiments in the mK range as well as stress dependent measurements. The binding energy and effective Bohr radius were determined for GaN, GaP, InP and GaAs and a weak exchange interaction between the hole and the Fe^{2+}center was detected.

Our results also provide insights into the hyperfine structure of the Fe^{3+} ground state, $^6A_1$: In GaP and InP, the Γ_8 level is found above the Γ_7 level.

Acknowledgement We thank Lars Podlowski and Torsten Wolf for carrying out the CAS experiments.

References

[1] R. P. Vaudo, X. Xu, A. Salant, J. Malcarne, and G. R. Brandes, phys. stat. sol. (a) **200**(1), 18–21 (2003).
[2] S. A. Wolf, D. D. Awschalom, R. A. Buhrman, J. M. Daughton, S. von Molnar, M. L. Roukes, A. Y. Chtchelkanova, and D. M. Treger, Science **294**(5546), 1488–1495 (2001).
[3] T. Dietl, H. Ohno, F. Matsukura, J. Cibert, and D. Ferrand, Science **287**(5455), 1019–1022 (2000).
[4] T. Jungwirth, J. Sinova, J. Masek, J. Kucera, and A. H. MacDonald, Rev. Mod. Phys. **78**(3), 809 (2006).
[5] H. Ohno, Science **281**(5379), 951–956 (1998).
[6] T. Dietl, H. Ohno, and F. Matsukura, Phys. Rev. B **63**(19), 195205 (2001).
[7] T. Dietl, phys. stat. sol. (b) **240**(2), 433–439 (2003).
[8] T. Graf, S. T. B. Goennenwein, and M. S. Brandt, phys. stat. sol. (b) **239**(2), 277–290 (2003).
[9] A. Bonanni, Semicond. Sci. Technol. **22**(9), R41–R56 (2007).
[10] C. Zener, Phys. Rev. **82**(3), 403 – 405 (1951).
[11] T. Dietl, F. Matsukura, and H. Ohno, Phys. Rev. B **66**(3), 033203 (2002).
[12] E. Malguth, A. Hoffmann, W. Gehlhoff, O. Gelhausen, M. R. Phillips, and X. Xu, Phys. Rev. B **74**(16), 165202 (2006).
[13] J. M. Langer and H. Heinrich, Phys. Rev. Lett. **55**, 1414 (1985).
[14] J. M. Langer, C. Delerue, M. Lannoo, and H. Heinrich, Phys. Rev. B **38**, 7723 (1988).
[15] I. Vurgaftman, J. R. Meyer, and L. R. Ram-Mohan, J. Appl. Phys. **89**(11), 5815–5875 (2001).
[16] S. H. Wei and A. Zunger, Appl. Phys. Lett. **72**(16), 2011–2013 (1998).
[17] P. Rinke, M. Scheffler, A. Qteish, M. Winkelnkemper, D. Bimberg, and J. Neugebauer, Appl. Phys. Lett. **89**(16), 161919 (2006).
[18] K. M. Yu, Z. Liliental-Weber, W. Walukiewicz, W. Shan, J. W. Ager, III, S. X. Li, R. E. Jones, E. E. Haller, H. Lu, and W. J. Schaff, Appl. Phys. Lett. **86**(7), 071910 (2005).
[19] B. K. Ridley, J. Phys. C, Solid State Phys. **13**(10), 2015–2026 (1980).
[20] B. K. Ridley and M. A. Amato, J. Phys. C, Solid State Phys. **14**(9), 1255–1269 (1981).
[21] M. A. Amato and B. K. Ridley, J. Phys. C, Solid State Phys. **13**(10), 2027–2040 (1980).
[22] W. C. Holton, J. Schneider, and T. L. Estle, Phys. Rev. **133**(6A), A1638–A1641 (1964).
[23] A. Zunger, Solid State Phys. **39**, 275 (1986).
[24] J. M. Baranowski, in: Deep Centers in Semiconductors, edited by S. T. Pantelides (Gordon and Breach, New York, 1986), p. 691.
[25] R. Heitz, A. Hoffmann, and I. Broser, Phys. Rev. B **45**(16), 8977–8988 (1992).
[26] S. Brehme, J. Phys. C, Solid State Phys. **18**(13), L319–L323 (1985).
[27] J. Baur, K. Maier, M. Kunzer, U. Kaufmann, and J. Schneider, Appl. Phys. Lett. **65**(17), 2211–2213 (1994).
[28] M. Godlewski and A. Zakrzewski, J. Phys. C, Solid State Phys. **18**(36), 6615–6625 (1985).
[29] H. Zimmermann, R. Boyn, and N. Nagel, phys. stat. sol. (b) **117**(1), 229–239 (1983).
[30] H. Lechner, D. M. Hofmann, B. K. Meyer, M. Azoulay, K. Krambrock, J. M. Spaeth, A. Dörnen, B. Kaufmann, M. S. P. Omling, and K. W. Benz, Adv. Mater. Opt. Electron. **3**(1–6), 223–232 (1994).
[31] W. Jantsch and G. Hendorfer, J. Cryst. Growth **101**(1–4), 404–413 (1990).
[32] A. J. Szadkowski, J. Phys.: Condens. Matter **2**(49), 9853–9859 (1990).
[33] J. Dieleman, J. W. de Jong, and T. Meijer, J. Chem. Phys. **45**(9), 3178–3184 (1966).
[34] B. V. Shanabrook, P. B. Klein, and S. G. Bishop, Physica B **116**, 444 (1983).
[35] We observed the $Fe^{2+}(^5E \rightarrow {}^5T_2)$ transition in ZnO by Fourier transform infrared transmission spectroscopy at 395 meV (to be published).
[36] U. Gerstmann, A. T. Blumenau, and H. Overhof, Phys. Rev. B **63**(7), 075204 (2001).
[37] M. Wegscheider, C. Simbrunner, H. Przybylinska, M. Kiecana, M. Sawicki, A. Navarro-Quezada, H. Sitter, W. Jantsch, T. Dietl, and A. Bonanni, phys. stat. sol. (a) **204**(1), 86–91 (2007).
[38] K. Sato and H. Katayama-Yoshida, Jpn. J. Appl. Phys. **40**(5B), L485–L487 (2001).
[39] M. Herbich, A. Twardowski, D. Scalbert, and A. Petrou, Phys. Rev. B **58**(11), 7024–7034 (1998).
[40] U. Kaufmann and J. Schneider, Festkörperprobleme: Advances in Solid State Physics (Vieweg, Braunschweig, 1980), p. 87.
[41] K. Maier, M. Kunzer, U. Kaufmann, J. Schneider, B. Monemar, I. Akasaki, and H. Amano, Mater. Sci. Forum **143–147**, 93–97 (1994).
[42] W. Gehlhoff, D. Azamat, U. Haboeck, and A. Hoffmann, Physica B **376/377**, 486–490 (2006).
[43] H. A. Jahn and E. Teller, Proc. R. Soc. Lond. A, Math. Phys. Sci. **161**(905), 220 (1937).
[44] T. Buch, B. Clerjaud, B. Lambert, and P. Kovacs, Phys. Rev. B **7**(1), 184 – 191 (1973).
[45] A. Hoffmann, R. Heitz, and I. Broser, Phys. Rev. B **41**(9), 5806–5816 (1990).
[46] K. Pressel, G. Bohnert, A. Dörnen, B. Kaufmann, J. Denzel, and K. Thonke, Phys. Rev. B **47**(15), 9411–9417 (1993).

[47] B. Kaufmann, A. Dörnen, and F. S. Ham, in: 23rd International Conference on the Physics of Semiconductors, Berlin 1996, Vol. 4, edited by M. Scheffler and R. Zimmermann (World Scientific, Singapore, 1996), p. 2829.
[48] K. Pressel, G. Bohnert, G. Rückert, A. Dörnen, and K. Thonke, J. Appl. Phys. **71**(11), 5703–5705 (1992).
[49] R. Heitz, P. Thurian, I. Loa, L. Eckey, A. Hoffmann, I. Broser, K. Pressel, B. K. Meyer, and E. N. Mokhov, Appl. Phys. Lett. **67**(19), 2822–2824 (1995).
[50] J. Baur, K. Maier, M. Kunzer, U. Kaufmann, J. Schneider, H. Amano, I. Akasaki, T. Detchprohm, and K. Hiramatsu, Appl. Phys. Lett. **64**(7), 857–859 (1994).
[51] D. Boulanger, D. Curie, and R. Parrot, J. Lumin. **48/49**, 680–684 (1991).
[52] W. A. Harrison, Phys. Rev. B **8**(10), 4487 (1973).
[53] C. K. Jørgensen, Discuss. Faraday Soc. **26**, 110–115 (1958).
[54] P. Thurian, A. Hoffmann, L. Eckey, P. Maxim, R. Heitz, I. Broser, K. Pressel, B. K. Meyer, J. Schneider, J. Bauer, and M. Kunzer, in: III–V Nitrides, Symposium, Boston 1996, edited by F. Ponce, T. Moustakas, I. Akasaki, and B. Monemar (Mater. Res. Soc., 1997), p. 707.
[55] W. C. Holton, M. de Wit, T. L. Estle, B. Dischler, and J. Schneider, Phys. Rev. **169**(2), 359–372 (1968).
[56] B. Bleaney and R. S. Trenam, Proc. R. Soc. Lond. A **223** (April), 1–14 (1954).
[57] A. Räuber and J. Schneider, Z. Naturforsch. A **17**, 266–270 (1962).
[58] J. Schneider, Z. Naturforsch. A **17**, 189 (1962).
[59] W. M. Walsh and L. W. Rupp, Phys. Rev. **126**(3), 952–955 (1962).
[60] W. Teuerle, E. Blaschke, and A. Hausmann, Z. Phys. A **270**(1), 37–41 (1974).
[61] M. de Wit and T. L. Estle, Phys. Rev. **132**(1), 195–201 (1963).
[62] G. H. Stauss, J. J. Krebs, and R. L. Henry, Phys. Rev. B **16**(3), 974 (1977).
[63] T. L. Estle, Phys. Rev. **136**(6A), A1702–A1704 (1964).
[64] J. C. Hensel, Bull. Am. Phys. Soc. **9**, 244 (1964).
[65] J. Lambe, J. Baker, and C. Kikuchi, Phys. Rev. Lett. **3**(6), 270–271 (1959).
[66] G. Brunthaler, U. Kaufmann, and J. Schneider, J. Appl. Phys. **56**(10), 2974–2976 (1984).
[67] R. S. Title, Phys. Rev. **131**(2), 623–627 (1963).
[68] P. Koidl, phys. stat. sol. (b) **74**(2), 477–484 (1976).
[69] R. Heitz, P. Maxim, L. Eckey, P. Thurian, A. Hoffmann, I. Broser, K. Pressel, and B. K. Meyer, Phys. Rev. B **55**(7), 4382–4387 (1997).
[70] U. W. Pohl, A. Ostermeier, W. Busse, and H. E. Gumlich, Phys. Rev. B **42**(9), 5751–5758 (1990).
[71] R. Parrot, A. Geoffroy, C. Naud, W. Busse, and H. E. Gumlich, Phys. Rev. B **23**(10), 5288–5300 (1981).
[72] K. Pressel, G. Rückert, A. Dörnen, and K. Thonke, Phys. Rev. B **46**(20), 13171–13178 (1992).
[73] K. Pressel, A. Dörnen, G. Rückert, and K. Thonke, Phys. Rev. B **47**(24), 16267–16273 (1993).
[74] E. Malguth, A. Hoffmann, M. Phillips, and W. Gehlhoff, Mater. Res. Soc. Symp. Proc. **892**, 131–136 (2006).
[75] E. E. Vogel, O. Mualin, M. A. de Orúe, and J. Rivera-Iratchet, Phys. Rev. B **44**(4), 1579–1587 (1991).
[76] E. E. Vogel, O. Mualin, M. A. de Orúe, J. Rivera-Iratchet, M. L. Flores, U. W. Pohl, H. J. Schulz, and M. Thiede, Phys. Rev. B **50**(8), 5231 (1994).
[77] H. J. Schulz, M. Thiede, U. W. Pohl, J. Rivera-Iratchet, M. A. de Orúe, M. L. Flores, O. Mualin, and E. E. Vogel, Z. Phys. B, Condens. Matter **98**(2), 215–221 (1995).
[78] O. Mualin, E. E. Vogel, M. A. de Orúe, L. Martinelli, G. Bevilacqua, and H. J. Schulz, Phys. Rev. B **65**(3), 035211 (2001).
[79] W. Low and M. Weger, Phys. Rev. **118**(5), 1119–1130 (1960).
[80] G. A. Slack, F. S. Ham, and R. M. Chrenko, Phys. Rev. B **152**(1), 376–402 (1966).
[81] F. S. Ham and G. A. Slack, Phys. Rev. B **4**(3), 777–798 (1971).
[82] G. A. Slack and B. M. O'Meara, Phys. Rev. **163**(2), 335 (1967).
[83] E. Malguth, A. Hoffmann, and X. Xu, Phys. Rev. B **74**(16), 165201 (2006).
[84] G. Rückert, K. Pressel, A. Dörnen, K. Thonke, and W. Ulrici, Phys. Rev. B **46**(20), 13207–13214 (1992).
[85] K. Pressel, K. Thonke, A. Dörnen, and G. Pensl, Phys. Rev. B **43**(3), 2239 (1991).
[86] W. H. Koschel, U. Kaufmann, and S. G. Bishop, Solid State Commun. **21**(12), 1069–1072 (1977).
[87] K. Thonke, K. Pressel, H. U. Hermann, and A. Dörnen, Mater. Sci. Forum **38–41**, 869–873 (1989).
[88] J. M. Baranowski, J. W. Allen, and G. L. Pearson, Phys. Rev. **160**(3), 627–692 (1967).
[89] J. H. Haanstra, in: International Conference on II–VI Semiconductor Compounds, edited by D. G. Thomas (W. A. Benjamin, New York, 1967), pp. 207–214.
[90] G. Roussos, H. J. Schulz, and M. Thiede, J. Lumin. **31/32** (Part 1), 409–411 (1984).
[91] D. Buhmann, H. J. Schulz, and M. Thiede, Phys. Rev. B **24**(11), 6221–6233 (1981).
[92] K. Pressel, Ph.D. thesis, Universität Stuttgart (1985).
[93] M. V. Klein, in: Light Scattering in Solids I, edited by M. Cardona (Springer, Berlin, 1975), p. 179.
[94] G. Goetz and H. J. Schulz, J. Lumin. **40/41**, 415–416 (1988).
[95] G. A. Slack, S. Roberts, and F. S. Ham, Phys. Rev. **155**(2), 170–177 (1967).
[96] M. Skowronski and Z. Liro, J. Phys. C, Solid State Phys. **15**(1), 137–145 (1982).
[97] S. A. Kazanskii, A. I. Ryskin, and G. I. Khil'ko, Opt. Spektrosk. **27**(2), 296 (1969).
[98] M. K. Udo, M. Villeret, I. Miotkowski, A. J. Mayur, A. K. Ramdas, and S. Rodriguez, Phys. Rev. B **46**(12), 7459–7468 (1992).
[99] K. Pressel, K. Thonke, and A. Dörnen, in: 20th Int. Conf. Phys. Semic., Thessaloniki 1990, Vol. 1, edited by E. M. Anastassakis and J. D. Joannopoulos (World Scientific, Singapore, 1990), p. 690.
[100] L. Podlowski, R. Heitz, P. Thurian, A. Hoffmann, and I. Broser, J. Lumin. **48**, 252–256 (1994).
[101] C. Testelin, C. Rigaux, A. Mauger, A. Mycielski, and C. Julien, Phys. Rev. B **46**(4), 2183–2192 (1992).
[102] J. T. Vallin, G. A. Slack, and C. C. Bradley, Phys. Rev. B **2**(11), 4406–4413 (1970).

[103] C. L. West, W. Hayes, J. F. Ryan, and P. J. Dean, J. Phys. C, Solid State Phys. **13**(30), 5631–5643 (1980).
[104] M. Villeret, S. Rodriguez, and E. Kartheuser, Phys. Rev. B **43**(4), 3443–3449 (1991).
[105] S. W. Biernacki, phys. stat. sol. (b) **102**(1), 235 (1980).
[106] L. Martinelli, G. Bevilacqua, J. Rivera-Iratchet, M. A. de Orúe, O. Mualin, E. E. Vogel, and J. Cartes, Phys. Rev. B **62**(16), 10873–10881.
[107] J. Rivera-Iratchet, M. A. de Orúe, and E. E. Vogel, Phys. Rev. B **34**(6), 3992 (1986).
[108] M. A. de Orúe, J. Rivera-Iratchet, and E. E. Vogel, J. Cryst. Growth **86**(1–4), 28–32 (1990).
[109] E. E. Vogel, J. Rivera-Iratchet, and M. A. de Orúe, Phys. Rev. B **38**(5), 3556 (1988).
[110] J. Rivera-Iratchet, M. A. de Orúe, M. L. Flores, and E. E. Vogel, Phys. Rev. B **47**(16), 10164 (1993).
[111] L. Martinelli, G. Bevilacqua, E. E. Vogel, and O. Mualin, Phys. Rev. B **65**(15), 155203 (2002).
[112] E. E. Vogel, O. Mualin, H. J. Schulz, and M. Thiede, Z. Phys. Chem. **201**(1–2), 99–109 (1997).
[113] M. Villeret, S. Rodriguez, and E. Kartheuser, J. Appl. Phys. **67**(9), 4221–4232 (1990).
[114] E. E. Vogel, M. A. de Orúe, J. Rivera-Iratchet, and J. E. Morales, J. Cryst. Growth **101**(1–4), 470–473 (1990).
[115] A. Karipidou, H. Nelkowski, and G. Roussos, J. Cryst. Growth **59**(1–2), 307–311 (1982).
[116] H. Nelkowski, O. Pfutzenreuter, and W. Schrittenlacher, J. Lumin. **17**(4), 419–423 (1978).
[117] K. P. O'Donnell, K. M. Lee, and G. D. Watkins, J. Phys. C, Solid State Phys. **16**(20), L723–L728 (1983).
[118] U. Kaufmann and J. Schneider, Solid State Commun. **21**(12), 1073–1075 (1977).
[119] T. L. Estle and W. C. Holton, Phys. Rev. **150**(1), 159–167 (1966).
[120] R. Kernocker, K. Lischka, and L. Palmetshofer, J. Cryst. Growth **86**(1–4), 625–628 (1990).
[121] A. Juhl, A. Hoffmann, D. Bimberg, and H. J. Schulz, Appl. Phys. Lett. **50**(18), 1292–1294 (1987).
[122] A. H. A. Wysmolek, Acta Phys. Pol. A **77**, 67 (1990).
[123] T. Wolf, D. Bimberg, and W. Ulrici, Phys. Rev. B **43**(12), 10004 (1991).
[124] K. Thonke and K. Pressel, Phys. Rev. B **44**(24), 13418–13425 (1991).
[125] A. Dörnen, K. Pressel, G. Rückert, and K. Thonke, Mater. Sci. Forum **143–147**(2), 791–795 (1994).
[126] K. Pressel, G. Rückert, K. Thonke, and A. Dörnen, in: 16th Int. Conf. Defects Semicond., edited by G. Davis, G. G. DeLeo, and M. Stavola, Mater. Sci. Forum **83–87**, 695 (1991).
[127] A. Baldereschi and N. O. Lipari, Phys. Rev. B **9**(4), 1525 (1974).
[128] V. N. Fleurov and K. A. Kikoin, Solid State Commun. **42**(5), 353–357 (1982).
[129] J. M. Noras and J. W. Allen, J. Phys. C, Solid State Phys. **13**(18), 3511–3521 (1980).
[130] R. Heitz, A. Hoffmann, and I. Broser, Phys. Rev. B **48**(12), 8672–8682 (1993).
[131] R. Dingle, Phys. Rev. Lett. **23**(11), 579–581 (1969).
[132] R. Heitz, A. Hoffmann, P. Thurian, and I. Broser, J. Phys.: Condens. Matter **4**(1), 157–168 (1992).
[133] T. Wolf, W. Ulrici, D. Côte, B. Clerjaud, and D. Bimberg, Mater. Sci. Forum **143–147**, 317 (1994).
[134] A. Bobyl and M. Sheinkman, Sov. Phys.-Semicond. **13**(11), 1296 (1979).
[135] V. Abakumov, V. Perel, and I. Yassievich, in: Nonradiative recombination in semiconductors, edited by V. M. Agranovich and A. Maradudin, Modern Problems in Condensed Matter Sciences, Vol. 33 (North-Holland, Amsterdam, 1991).
[136] E. A. Pashitskii and S. M. Ryabchenko, Sov. Phys. Solid State **21**(2), 322–323 (1979).
[137] T. Jungwirth, W. A. Atkinson, B. H. Lee, and A. H. Mac Donald, Phys. Rev. B **59**(15), 9818–9821 (1999).
[138] H. Ohno, J. Magn. Magn. Mater. **200**, 110–129 (1999).
[139] S. J. Potashnik, K. C. Ku, R. Mahendiran, S. H. Chun, R. F. Wang, N. Samarth, and P. Schiffer, Phys. Rev. B **66**(1), 012408 (2002).
[140] M. Linnarsson, E. Janzén, B. Monemar, M. Kleverman, and A. Thilderkvist, Phys. Rev. B **55**(11), 6938–6944 (1997).
[141] L. Podlowski, A. Hoffmann, and I. Broser, J. Cryst. Growth **117**(1–4), 698–703 (1992).
[142] T. Wolf, Ph.D. thesis, Technische Universität Berlin (1992).
[143] S. Rodriguez, P. Fisher, and F. Barra, Phys. Rev. B **5**(6), 2219 (1972).
[144] F. S. Hickernell and W. R. Gayton, J. Appl. Phys. **37**(1), 462 (1966).
[145] G. Weber and W. Ruhle, phys. stat. sol. (b) **92**(2), 425–431 (1979).
[146] O. Madelung (ed.), Physics of Group IV Elements and III–V Compounds, Landolt–Börnstein: Numerical Data and Functional Relationships in Science and Technology, Group III: Crystal and Solid State Physics, Vol. 17a (Springer-Verlag, Berlin, 1982).
[147] G. F. Koster, J. O. Dimmock, R. G. Wheeler, and H. Statz, Properties of the Thirty-two Point Groups (M.I.T. Press, Cambridge, Massachusetts, 1963).
[148] J. B. Xia, K. W. Cheah, X. L. Wang, D. Z. Sun, and M. Y. Kong, Phys. Rev. B **59**(15), 10119–10124 (1999).
[149] C. Schrepel, U. Scherz, W. Ulrici, and K. Thonke, Mater. Sci. Forum **258–263**, 1075–1080 (1997).
[150] P. Thurian and A. Hoffmann, in: XIV Int. Symp. Electron–Phonon Dynamics and Jahn–Teller-Effect, Erice, 1998, edited by G. Bevilacqua, L. Martinelli, and N. Terzi (World Scientific, Singapore, 1998), pp. 216–229.
[151] C. Goebel, C. Schrepel, U. Scherz, P. Thurian, G. Kaczmarczyk, and A. Hoffmann, Mater. Sci. Forum **258–263**(2), 1173–1178 (1997).
[152] C. Bundesmann, N. Ashkenov, M. Schubert, D. Spemann, T. Butz, E. M. Kaidashev, M. Lorenz, and M. Grundmann, Appl. Phys. Lett. **83**(10), 1974–1976 (2003).
[153] F. J. Manjon, B. Mari, J. Serrano, and A. H. Romero, J. Appl. Phys. **97**(5), 053516 (2005).

